Thesis

Parameters Determining Intercept Capabilities; SM-3 Versus Various Threat Ranges

---

Author
SLt N. (Noah) Stam (366925)

Supervisors
Dr. ir. R. Savelsberg
Prof. dr. ir. M. Voskuijl

A thesis submitted in partial fulfillment of the
requirements for the degree Bachelor of Science in
Military Systems & Technology

Major in Aeronautical Engineering

Faculty of Military Sciences

Netherlands Defence Academy

April 2021

Abstract

Ballistic missile defence is vital for protecting assets and population from conventional as well as nuclear ballistic threats. To do so, interceptor missiles are used to kinetically negate ballistic targets outside of the atmosphere. However, due to uncertainties in the measured target trajectory, the kill vehicle (KV) will have to adjust its course during the final phase of engagement to achieve an intercept. The present research focuses on performing ballistic missile defence from warships using the Standard Missile 3 (SM-3) interceptor missile. This paper answers the question as to what extent geometry and closing velocity affect the SM-3 KV's total divert and lateral acceleration needed for an intercept. Besides, it includes answers on the strategic significance of the FTM-44 ballistic missile defence test conducted by the U.S. Navy on November 16, 2020, in which a ballistic missile dummy target was intercepted by an SM-3's kill vehicle launched from the Arleigh Burke-class destroyer USS John Finn.

In order to formulate these answers, a literature review was conducted in which feasible KV parameters were estimated based on public sources, including divert capacity and infrared seeker range. In addition, the FTM-44 flight test was investigated by means of the navigational warning areas issued prior to the event. From this, it was concluded that a rather favourable intercept geometry was adopted during the test. After this, a variety of simulations of ballistic missile engagements was conducted. Hereby, several relations between intercept parameters were derived. These parameters include closing velocity, intercept geometry, target offset, infrared seeker range and divert capacity. Using the derived parameter relations, it was concluded that the FTM-44 scenario could not have been a success under the circumstances expected from a typical ballistic missile engagement. That the test was a success nonetheless can be addressed to the expedient intercept geometry in combination with a relatively easy target. Therefore, it was found that the FTM-44 flight event does not represent strategic significance concerning the problem of U.S. ballistic missile defence. The present research was limited to the use of public information only. Nevertheless, it forms a framework for future research for which more specific and official knowledge on the topic is available.

Acknowledgements

Firstly, I would like to thank Dr. Ralph Savelsberg for being the most dedicated and understanding supervisor. Throughout our cooperation over the last months, he infected me with his great enthusiasm for the topic; really making me want to get the best out of this paper. I can easily state that without him, this work would not have been possible.

Next, I would like to thank Drs. Laetis Kuipers, together with Nikki Lanning for helping me with perfectioning my use of the English language while writing this paper. Their efforts made sure that I was able to communicate my train of thought and findings more clearly. Moreover, I believe that this study is more valuable in English than Dutch.

Lastly, I would like to mention my unofficial external supervisor James Kiessling. His extensive knowledge has allowed me to understand the matter more thoroughly. More specifically, his help on the topics of infrared signatures and sensors was most helpful. Our correspondance helped me stay sharp and at the same time gave me the possibility to exchange thoughts on my day's work. This was much appreciated, especially due to the COVID-19 situation, which had me working from home.

Contents

List of Tables

List of Figures

List of Abbreviations and Symbols

Abbreviations

ACS Attitude Control System

BM Ballistic Missile

BMD Ballistic Missile Defence

DACS Divert and Attitude Control System

DCS Divert Control System

ENU East-North-Up local coordinate system

ICBM Intercontinental Ballistic Missile

IR Infrared

IRBM Intermediate Range Ballistic Missile

KV Kill Vehicle

LOS Line-of-Sight

MDA U.S. Missile Defense Agency

MRBM Medium Range Ballistic Missile

NEFD Noise Equivalent Flux Density

PIP Predicted Intercept Point

RV Re-entry Vehicle

SDACS Solid Divert and Attitude Control System

SM-3 Standard Missile 3

SRBM Short Range Ballistic Missile

TDACS Throttling Divert and Attitude Control System

VLS Vertical Launching System

Symbols

A	Surface area	$\mathrm{m^2}$
E	Flux per unit area at the detector	$\mathrm{W\,m^{-2}}$
f	Propellant fraction used for divert	-
F	Infrared sensor bandwidth correction	-
g	Gravitational acceleration	$\mathrm{m\,s^{-2}}$
GM	Standard gravitational parameter	$\mathrm{m^3\,s^{-2}}$
I_{sp}	Specific impulse	s
m	Mass	kg
$\dot{m}$	Mass flow rate	$\mathrm{kg\,s^{-1}}$
$\overline{M}$	Molar mass	$\mathrm{g\,mol^{-1}}$
n	Lateral acceleration due to guidance perpendicular to LOS	$\mathrm{m\,s^{-2}}$
N	Effective navigation ratio	-
o	Target offset	m
r	Distance to the centre of the Earth	m
R	Range	m
S/N	Signal-to-noise ratio	-
t	Time	s
T	Temperature	K
Tc	First order KV system time constant	s
V	Velocity	$\mathrm{m\,s^{-1}}$
x	In the local horizontal direction east	m
x'	In the local horizontal direction parallel to target and interceptor trajectories	m
y	In the local horizontal direction north	m
z	In the local vertical direction	m
γ	Flight path angle	rad
δ	Dimensionless ballistic trajectory parameter	-
ΔV	Total divert	$\mathrm{m\,s^{-1}}$
ϵ	Emissivity	-
θ	Direction of missile position in 2D polar coordinate system	rad
λ	Line-of-sight	rad
Λ	Wavelength	m
σ	Stefan-Boltzmann constant $5.67 \cdot 10^{-8}$	$\mathrm{W\,m^{-2}\,K^{-4}}$
τ	Thrust	N

Subscript

$\perp$	Perpendicular to	
$\oplus$	Earth	
0	Initial condition	
a	Actual	
bo	Burnout	
c	Closing	
com	At combustion	
d	Demanded	
h	Horizontal component	
i	Initial	

ID	Identification
IR	Infrared
M	Missile
min	Minimum
max	Maximum
p	Predicted
$prop$	Propellant
PIP	Predicted intercept point
$proj$	Projected
T	Target
TM	Difference between target and missile
v	Vertical component
x	In the local horizontal direction east
x'	In the local horizontal direction parallel to target and interceptor trajectories
y	In the local horizontal direction north
z	In the local vertical direction

1. Introduction

Ballistic missiles (BMs) are defined as rocket-propelled self-guided strategic weapon systems that follow a ballistic trajectory to deliver a payload from their launch site to a predetermined target [1]. BMs have formed a threat ever since World War II when Nazi-Germany developed the first BM, the V-2. Although limited in accuracy, the V-2's operational range of 320 km was sufficient to hit U.K. targets from the European mainland. Ever since, BMs have developed rather quickly. Today, there are BMs that are capable of eliminating targets exceeding distances of 15,000 km to launch site.

BMs are usually categorised by range. On one end of the spectrum, short range ballistic missiles (SRBMs) cover ranges up to 1,000 km. Whereas, intercontinental ballistic missiles (ICBMs) have a range of 5,500 km and more. The scope between these ranges is covered in Table 1.1.

Table 1.1: Overview of BM categories based on operational range.

BM category	Ground range (km)
Short Range Ballistic Missiles (SRBMs)	<1,000
Medium Range Ballistic Missiles (MRBMs)	1,000 - 3,500
Intermediate Range Ballistic Missiles (IRBMs)	3,500 - 5,500
Intercontinental Ballistic Missiles (ICBMs)	>5,500

The lower end of BM ranges includes tactical weapons as long range unmanned artillery. Longer range missiles in the past only held roles for nuclear weapon delivery. However, with the introduction of precision terminal guidance it is also feasible to use conventional payloads on longer range missiles. In order to protect assets and population from tactical strikes (SRBM) as well as strategic nuclear threats (ICBM) and anything in-between, ballistic missile defence (BMD) is of great importance. One way to perform BMD is by performing so-called exo-atmospheric interceptions: intercepting a BM's re-entry vehicle (RV) outside of the atmosphere. This can be accomplished with either ground-based interceptors or much smaller warship based launchers. An example of such a ship based launcher optimised for outside atmosphere interceptions is the Standard Missile 3 (SM-3). After detecting an incoming threat, a predicted intercept point (PIP) is determined using radar observations or satellite data. The PIP indicates the point where the interceptor's trajectory intersects with the predicted target trajectory, both in time and space. The SM-3 is then launched from a vertical launching system (VLS) following the calculated trajectory. After cutting off its three rocket stages, the remaining kinetic kill vehicle (KV) (see Figure 1.1) has a velocity $\vec{V}_{M,PIP}$. Ideally, this $\vec{V}_{M,PIP}$ will lead the KV directly to the RV.
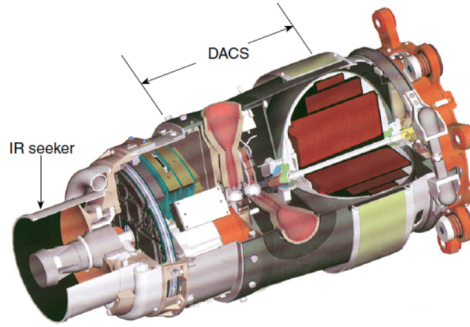
Figure 1.1: SM-3 exo-atmospheric kill vehicle [2].

However, due to limitations in radar accuracy and change of target impulse introduced by engine cutoffs, the PIP and the actual intercept point will likely be offset (see Figure 1.2). To compensate for this offset, the KV uses its infrared (IR) seeker and a built-in Divert and Attitude Control System (DACS). The DACS consists of several thrusters that use rocket fuel to change the KV's attitude and lateral acceleration, and therefore its direction of velocity. This way, if all goes according to plan, the KV will hit the incoming threat, resulting in a successful interception.
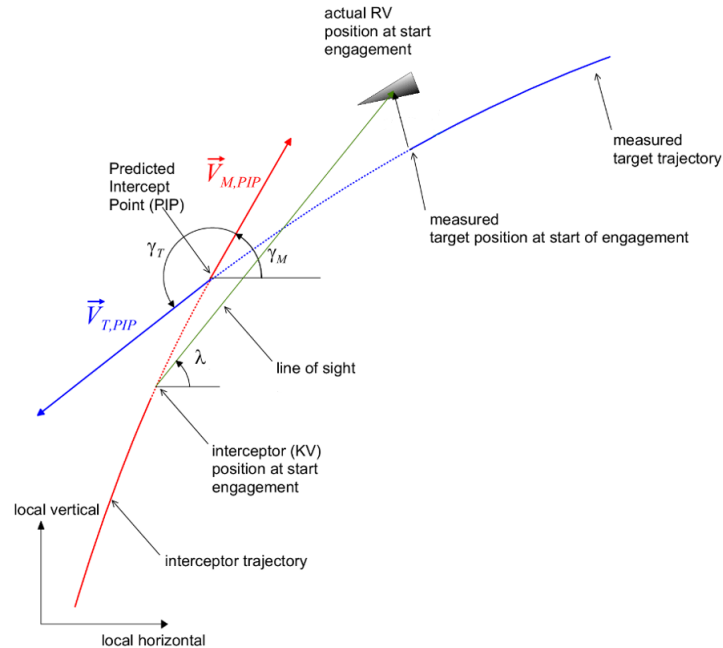
Figure 1.2: 2D geometry of an exo-atmospheric ballistic missile intercept [3].

On November 16, 2020, such an interception was demonstrated by the U.S. Navy, during the FTM-44 BMD test. A dummy ICBM was launched from the Ronald Reagan Ballistic Missile Defense Test Site on Kwajalein, North Pacific. Subsequently, the dummy ICBM's RV was intercepted by an SM-3 Block IIA launched from an Arleigh Burke-class destroyer [4]. It proved possible to negate an ICBM using an SM-3 Block IIA, despite the fact that this missile was only designed to intercept targets up to intermediate range ballistic missiles (IRBMs) (see Table 1.1). Since ICBMs have higher velocities than IRBMs and the KV's seeker is designed against less stressing problems, there is less time for the KV to adjust its trajectory to actually hit the target. In addition, due to the

greater altitude of ICBMs, they are more likely to be out of interceptor range for most of their flight. Nevertheless, the U.S. Missile Defense Agency (MDA) claims to have proven that the SM-3 Block IIA also suffices as a means of eliminating ICBM threats. According to MDA Director Vice Admiral Jon Hill, it has been "demonstrated that an Aegis BMD-equipped vessel equipped with the SM-3 Block IIA missile can defeat an ICBM-class target" [5].

However, an animation of the conducted test released by the MDA shows that the interceptor approached its target from the side or even in a tail-chase[1] rather than head-on, hereby limiting the closing velocity[2] and giving the KV more time to adjust its course. This might very well have affected the lateral acceleration and total divert[3] needed for an intercept. Figure 1.3 shows a screenshot of the animation that clearly depicts both the interceptor's and the ICBM's trajectory.
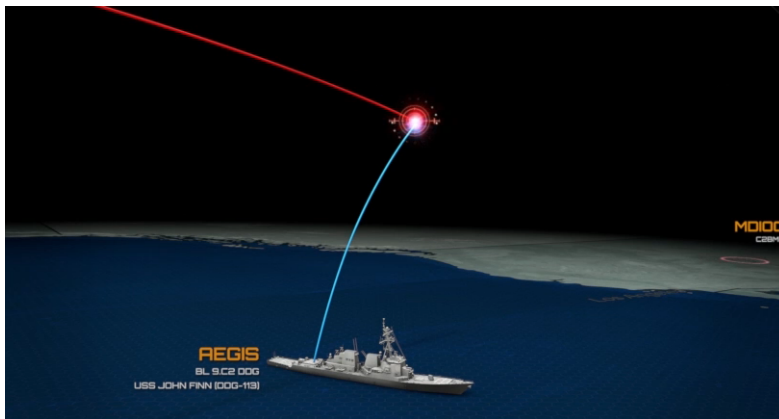
Figure 1.3: MDA animation of FTM-44 ICBM intercept using SM-3 Block IIA [6].

The current study aims to determine how and to what extent geometry and closing velocity affect the KV's chances of successfully eliminating a ballistic threat, and thus whether reservations need to be made when it comes to the meaning of the statement made by Vice Admiral Hill. In other words, the research question concerns *to what extent the outcome of the FTM-44 test poses strategic significance concerning the problem of U.S. BMD.*

Previous claims that an SM-3 was suitable for intercepting ICBMs prompted an earlier study which included intercepts in three dimensions and detailed modelling of the SM-3 Block IA DACS system [7]. This geometry made isolating the effects of changing various parameters a highly complex affair. Therefore, to answer the research question, the current study used numerical simulations in two (2D) as well as in three dimensions (3D), adopting a model with proportional navigation[4] as the guidance law. In addition, various engagements were simulated by changing the launch point of the interceptor, target velocity, KV IR range and the offset between the PIP and the actual target position.

---

[1]Engagement in which the target flies away from the interceptor.
[2]The negative time derivative of the target to missile distance.
[3]Lateral acceleration integrated over time.
[4]Guidance law based on constant line-of-sight as an interceptor approaches its target.

The paper starts with a theoretical background in the form of a literature review, including the topics of the SM-3 KV, target offset and the FTM-44 BMD test. The Methods section includes the models and simulations used. Next, the output of these simulations will be shown and discussed in the Results section. After this, a number of conclusions will be drawn concerning this study. Finally, limitations will be given, along with recommendations for possible future research.

2. Literature Review

Now that BMD and its relevance have been introduced, this chapter will dive deeper into the theory on the matter, starting with the KV and its subsystems. Next, the subject of target offset will be discussed and finally, the FTM-44 test will be investigated.

2.1 Kill Vehicle

The KV consists of several subsystems that make up the system as a whole. The basic components and their relations are illustrated in Figure 2.1. In this section, first the guidance law will be discussed. Next, the KV's DACS and IR seeker will be dealt with.
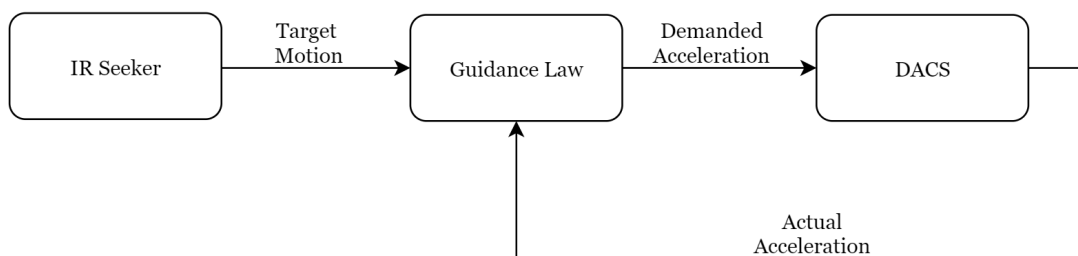
Figure 2.1: The KV system.

2.1.1 Proportional Navigation

As stated earlier, the PIP and the actual point of intercept will likely be offset. For the KV to be able to compensate for this offset, it has to 'know' how big this offset is and what acceleration is needed to countervail it. In this process, the line-of-sight (LOS), or λ, plays an important role. λ is defined as the angle between the local horizontal and the direction from the missile towards the target (see Figure 1.2). The rate (or first time derivative) of LOS ($\dot{\lambda}$) indicates the target offset at time t during engagement. $\dot{\lambda}$ in $[\frac{\text{rad}}{\text{s}}]$, together with the closing velocity V_c in $[\frac{\text{m}}{\text{s}}]$ and a constant parameter called the effective navigation ratio N, determine the demanded acceleration perpendicular to λ, n_d in $[\frac{\text{m}}{\text{s}^2}]$.

$$n_d = NV_c\dot{\lambda} \tag{2.1}$$

Equation 2.1 [8, p. 14] shows that for the case KV vs. RV, the KV's lateral acceleration demand will be proportional to the design constant N, V_c and $\dot{\lambda}$. Moreover, for a 3D intercept geometry, Equation 2.1 is divided into two components:

$$n_{d,v} = NV_c\dot{\lambda}_v \tag{2.2}$$

$$n_{d,h} = NV_c\dot{\lambda}_h \tag{2.3}$$

with $\dot{\lambda}_v$ and $\dot{\lambda}_h$ the vertical and horizontal components of $\dot{\lambda}$. $n_{d,v}$ and $n_{d,h}$ indicate the demanded lateral accelerations perpendicular to λ_v and λ_h, respectively. A more graphical explanation of this is depicted in Figure 2.2.
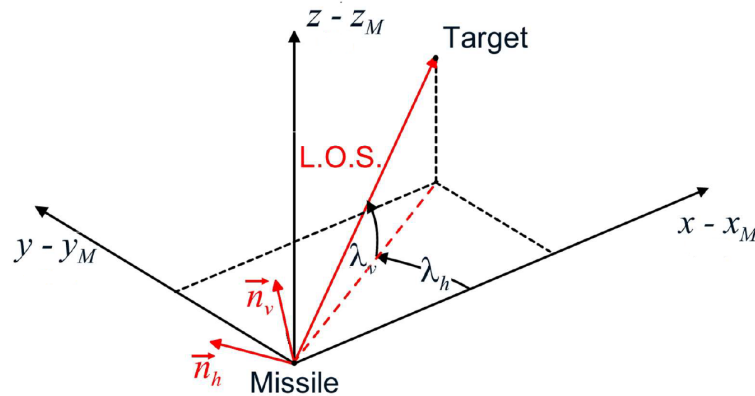
Figure 2.2: Lateral acceleration demands and LOS angles in 3D [7].

Note that in the case of a perfect flight control system and limitless acceleration capabilities, the launcher's KV will always hit its target. However, this is not the case in real life. Time is needed for the seeker measurements to be applied to determine angle rates $\dot{\lambda}$. Additionally, the flight control system as well as any mechanical component will introduce a delay as well. As for the divert capabilities: an SM-3 can only carry so much weight in flight because certain demands for operational range are to be met. Therefore, the KV cannot contain infinite amounts of fuel for its DACS.

2.1.2 Divert and Attitude Control System

The KV's DACS consists of two subsystems: the attitude control system (ACS) and the divert control system (DCS). The former of these uses six thrusters on the back of the vehicle to make sure the IR seeker points and stays pointed towards the incoming target. The latter provides the necessary lateral acceleration to put and keep the KV on collision course with its target. For this, the DCS uses four thrusters as illustrated in Figure 2.3.
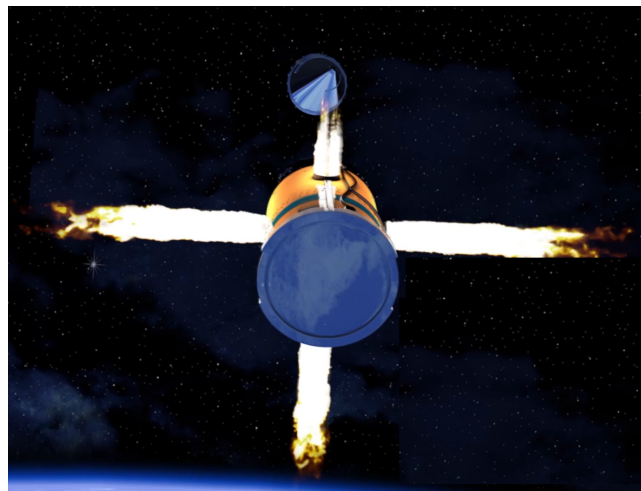
Figure 2.3: A cartoon of an SM-3 KV in terminal flight phase using its DACS [6].

The SM-3 Block IA uses a so-called Solid Divert and Attitude Control System (SDACS). This system burns its propellant in fixed grains, without being able to regulate the amount of thrust at a certain time. The SM-3 Block IA's successors, the SM-3 Block IB and IIA, are equipped with a Throttling Divert and Attitude Control System (TDACS) instead. Unlike the SDACS, this system is able to regulate, or throttle, the amount of thrust, hereby using the propellant available more efficiently than its predecessor. Also, the TDACS can generate higher thrust levels altogether. Since public information on the TDACS is very limited and most likely classified, the SDACS was used to determine the divert capabilities of the Block IA KV. The Block IA KV's capabilities were then used to estimate the Block IIA KV's divert capacity by means of simulating BM engagements. This will be discussed further in the Methods section.
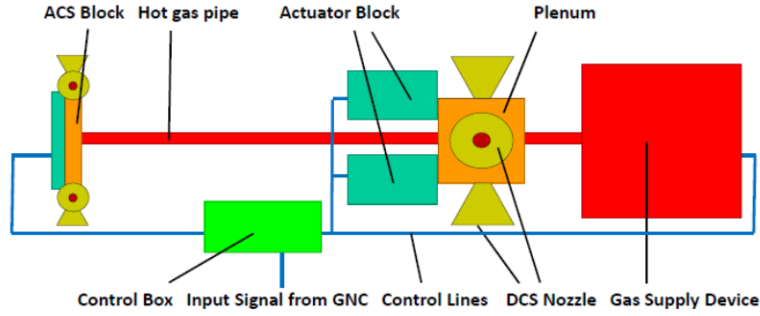
Figure 2.4: SDACS with a central gas generator [9].

To supply its thrusters, the SDACS is equipped with three solid Al-AP-HTPB [1] propellant grains [10]. Firstly, this propellant is fed into a central gas generator. The gas is then distributed to the different nozzles, depending on the thrust demanded by the actuators (see Figure 2.4). Nevertheless, the SDACS' DCS feeds every pair of opposite nozzles an equal share of gas flow regardless of the acceleration demands [7]. Also, every pair takes care of the divert in either $\vec{n}_h$ or $\vec{n}_v$ direction (see Figure 2.2). Therefore, the total divert (ΔV) available is fixed for each of these directions and not for the system as a whole. To determine the ΔV the DCS can generate per direction, the rocket equation was used.

$$\Delta V = g I_{sp} \ln \left(\frac{m_i}{m_i - f \cdot m_{prop}} \right) \tag{2.4}$$

In Equation 2.4, g is the gravitational acceleration at sea level 9.81 $\frac{\mathrm{m}}{\mathrm{s}^2}$. I_{sp} is the specific impulse in [s], m_i and m_{prop} are the vehicle's initial and total propellant's mass in [kg], respectively. Lastly, f indicates the propellant fraction used for divert by one pair of opposite DCS nozzles. Note that Equation 2.4 would give a lower estimate of the total divert because the change of the KV's mass due to the part of the propellant flow that is not used for the divert in the direction that is being considered, is being neglected. This is the gas flow through the ACS nozzles and the other pair of DCS nozzles. However, since the KV does not use a clean rocket engine, but a gas generator instead, it is likely that additional thermodynamical losses occur in the process. Nevertheless, the value for the gas generator's efficiency is unknown and therefore ignored in this research. Consequently, the values derived in this section are upper limits of the SDACS' capabilities instead of lower limits.

To solve Equation 2.4 for ΔV, first the propellant's I_{sp} is needed. For Al-AP-HTPB,

---

[1]Aluminium ammonium perchlorate hydroxyl-terminated polybutadiene.

$I_{sp} = 265$ s. However, this value only applies for a combustion temperature of 3480 K [10]. Since the nozzles will not be able to sustain this temperature in reality it is less, namely 2311 K [11]. Therefore, the I_{sp} will also be below 265 s. Frem [12, p. 2] cited that the I_{sp} is mostly affected by the propellant's combustion temperature T_{com} in [K] and molar mass $\overline{M}$ in $[\frac{g}{mol}]$ and that the approximate relationship between these parameters is given by Equation 2.5.

$$I_{sp} \propto \sqrt{\frac{T_{com}}{\overline{M}}} \tag{2.5}$$

To determine the total molar mass of the propellant, the value for each component is needed. This is: 2800 $\frac{g}{mol}$ for HTPB, 117.49 $\frac{g}{mol}$ for AP and 26.982 $\frac{g}{mol}$ for aluminium. Furthermore, the composition of the propellant is 12 wt% HTPB, 68 wt% AP and 20 wt% aluminium [13]. Combining the separate molar masses and the propellant's composition results in a total molar mass of $\overline{M} = 75.51$ $\frac{g}{mol}$. Using Equation 2.5 yields an $I_{sp} \approx 215.95$ s for $T_{com} = 2311$ K.

Now that the specific impulse of the SDACS propellant is known, m_i, m_{prop} and f are the only parameters left that are needed to solve Equation 2.4. Robinson [10] states that the KV carries 10 lbs propellant and that it has a total mass of 37 lbs. This means $m_i = 16.78$ kg and $m_{prop} = 4.54$ kg. Moreover, according to Naumann et al [9], ideally the ACS uses about 10% of the total amount propellant. This would result in $f = 0.9$. However, since Equation 2.4 approaches the total divert per direction, only half of the fuel should be included in the calculation. Considering this, $f = 0.5 \cdot 0.9 = 0.45$.

Substituting the derived values for I_{sp}, m_i, m_{prop} and f into Equation 2.4 yields a maximum Block IA SDACS' $\Delta V \approx 274.7$ $\frac{m}{s}$ for each of the two directions $\vec{n}_h$ and $\vec{n}_v$. Another constraint for the DACS is that of its maximum lateral acceleration. To determine this value, Equation 2.6 was used:

$$\tau_{max} = g I_{sp} \dot{m}_{max} \tag{2.6}$$

with $\dot{m}_{max}$ being the maximum propellant mass flow in $[\frac{kg}{s}]$ and τ_{max} the maximum amount of thrust in [N] per pair of opposite nozzles. According to Sullins [14] the DACS burns its second propellant grain for 10 s at target detection. This is also the grain which produces the highest thrust in order to put the KV on collision course with the target. Assuming it includes 80% of the 10 lbs total propellant, means 8 lbs is being burned during 10 s. This yields a total gas flow of $\dot{m}_{max} \approx 0.36$ $\frac{kg}{s}$. Be that as it may, this value is subject to the ratio f, just like for the ΔV capacity. Again using $f = 0.45$ yields $\dot{m}_{max} \approx 0.16$ $\frac{kg}{s}$. Substituting the values for g, I_{sp} and $\dot{m}_{max}$ into Equation 2.6 yields $\tau_{max} \approx 346$ N. Lastly, to determine the maximum lateral acceleration Newton's Second Law of Motion was used.

$$n_{max} = \frac{\tau_{max}}{m} \tag{2.7}$$

In Equation 2.7, n_{max} is the maximum value for n_v and n_h in $[\frac{m}{s^2}]$ and m indicates the vehicle's mass in [kg]. Since the maximum acceleration will be achieved during the start of the engagement, it is reasonable to consider the vehicle's mass to be its initial mass minus half of the propellant's mass burned during this period of maximum thrust. That is $37 - 4 = 33$ lbs or 15 kg. Substituting this value into Equation 2.7, together with τ_{max} yields $n_{max} \approx 23.1$ $\frac{m}{s^2}$ for the Block IA's SDACS.

The Block IIA TDACS' capabilities were determined by means of simulations. These simulations will be discussed further in the Methods section.

2.1.3 IR Seeker

After the KV separated from the SM-3's final rocket stage, the ACS points the IR seeker (see Figure 1.1) in the direction where the target is most likely to be. The seeker is then used to detect, identify and track the target. Little has been published on the capabilities of this instrument, and therefore an educated guess will be made on the IR seeker range. The following expression can be derived for the IR incidence E in $[\frac{\text{W}}{\text{m}^2}]$ at a distance R in [m] from the source:

$$E = \frac{\epsilon A_{proj} \sigma T^4 F}{\pi R^2} \tag{2.8}$$

with A_{proj} being the projected target's surface area in the direction of the seeker in [m^2]. σ is the Stefan-Boltzmann constant of $5.67 \cdot 10^{-8}$ Wm^{-2}K^{-4}. ϵ corresponds to the target's emissivity compared to a black body equivalent. T is the source's temperature in [K], lastly, F denotes the part of the total target radiation that is within the seeker's bandwidth. The full derivation of Equation 2.8 is included in Appendix A.1.

Rewriting Equation 2.8 for the maximum IR range (for a fixed target signature) yields Equation 2.9.

$$R_{IR} = \sqrt{\frac{\epsilon A_{proj} \sigma T^4 F}{\pi E_{min}}} \tag{2.9}$$

According to Evans [15], RV temperature in [K] and emissivity times the projected area in [m^2] are distributed as depicted by the red triangles in Figure 2.5. From this scatterplot it can be derived that the target's ϵA_{proj} ranges from 1 up to 4 m^2. Secondly, RV temperatures range from 260 up to 380 K.
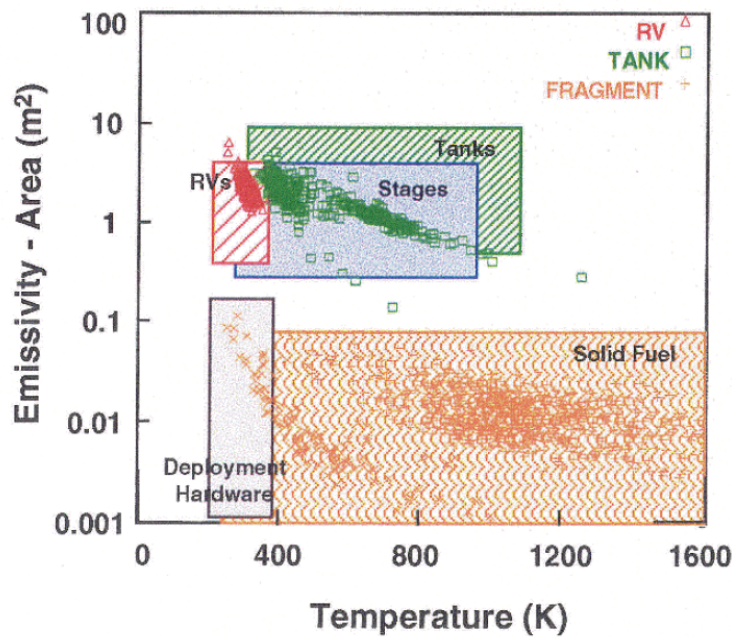
Figure 2.5: Target signatures [15].

The data in Figure 2.5 was derived from the THAAD [2] threat set including SRBMs/M-RBMs. ICBM signatures are significantly more challenging than those of MRBMs (and IRBMs) as ICBM RVs travel through space for a longer period of time and therefore cool down much more. Also, the application of an ascent shroud to protect the RV during boost eliminates ascent heating. When it comes to values for A_{proj}, ICBM RV warheads are often nuclear and consequently smaller than their conventional MRBM and IRBM counterparts. Considering this, the target signatures adopted for this research are as stated in Table 2.1.

Table 2.1: Adopted target signatures.

Signature	MRBMs/IRBMs	ICBMs
T [K]	300	270
ϵA_{proj} [m^2]	2	1.5
F [-]	0.4	0.3

Next, F follows from integrating Planck's Law over the sensor's bandwidth for a given target temperature. The universal black body curve in Figure 2.6 displays this integration in a single graph. Since the SM-3's seeker is a long wave infrared sensor, its bandwidth is either $6 - 12$ μm or $8 - 14$ μm. From these options, the former bandwidth is the best candidate for the KV IR seeker as it requires less internal cryogenic cooling. Assuming $6 - 12$ μm and applying Figure 2.6 for this bandwidth and the temperatures stated in Table 2.1 yields $F = 0.4$ and $F = 0.3$ for MRBM/IRBM and ICBM targets, respectively.
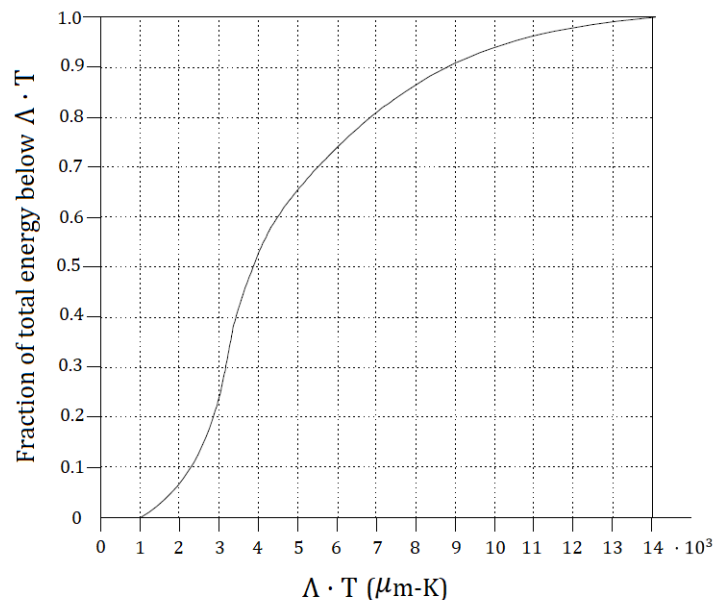
Figure 2.6: Universal black body curve [16].

Furthermore, E_{min} is defined as follows.

$$E_{min} = \text{S/N} \cdot \text{NEFD} \tag{2.10}$$

---

[2]Terminal High Altitude Area Defence

In Equation 2.10, S/N is the signal-to-noise ratio. This value determines the ratio between the target's radiation detected by the sensor and the external (environmental) plus internal noise. Secondly, NEFD is the noise equivalent flux density, which is defined as the incoming IR power per unit area at the aperture that would give an S/N of 1 at the sensor. For a 90% detection probability, the S/N required is 5.4 [17]. However, for the KV to identify its target in a cloud of decoys, separated rocket stages and debris, and subsequently gather sufficient track data for a divert, a higher accuracy is required. According to Pilgrim [18] this higher accuracy is a signal-to-noise ratio of S/N = 20. Moreover, for target ID and tracking a timeline of 2 s was adopted, as the topics of seeker resolution and target filtering were not included in this research.

Estimating the NEFD value can be challenging due to limited literature on the topic. Therefore, the following parameter space was used.

$$10^{-13} < \text{NEFD} < 10^{-9} \frac{\text{W}}{\text{m}^2}$$

The actual value for the SM-3 Block IA seeker's NEFD was determined by simulating standard scenarios, adopting the target signatures in Table 2.1 and S/N = 20. This will be further discussed in the Methods section. Nevertheless, substituting the values in Table 2.1, together with S/N = 20 into Equations 2.9 and 2.10 yields $R_{IR} \approx \frac{2.42 \cdot 10^{-3}}{\sqrt{NEFD}}$ km for MRBM/IRBM targets and $R_{IR} \approx \frac{1.47 \cdot 10^{-3}}{\sqrt{NEFD}}$ km for ICBM targets. Moreover, Lewis [19] claimed the Block IIA's seeker to be at least two times as sensitive as its predecessor, the Block IB seeker. Assuming that the latter has a sensor sensitivity of 25% better than that of the Block IA, the Block IIA sensor should have an NEFD of at least 2.5 times smaller than that of the Block IA. This was the value adopted for this research. Note that this is a rough estimate. However, the Block IIA's divert capacity was adopted based on its IR seeker range and in the end it is the combination between these two that makes up the actual intercept capabilities.

2.2 Target Offset

The distance between the PIP and the actual target position at the time of the predicted intercept is the target offset o. In order to determine how much divert is required for a certain intercept, it is necessary to know how big of a target offset to expect. Two scenarios are possible considering the target offset. The scenario in which the ground and/or space based assets can make an ID on the target and the scenario in which they cannot. In the former situation, the target offset is solely based on the external sensor's accuracy. In the latter, the offset will largely depend on the measurements of the cloud of potential targets. This cloud includes the actual RV, separated rocket stages, debris caused by the RV separation and in some cases also decoys. To stay on the safe side in regard of estimating the target offset, this is the scenario adopted in this research.

According to Lewis [20], a reasonable speed between two objects following separation is $5 \frac{\text{m}}{\text{s}}$. In the worst case scenario, this speed would be aimed completely in either the $\vec{n}_h$ or $\vec{n}_v$ direction (see Figure 2.2) because then the KV would have only one pair of nozzles to compensate for the offset. This is the scenario that was adopted, applying a target offset of $5 \cdot t_{RV}$ [m] for both the $\vec{n}_h$ and $\vec{n}_v$ direction. With t_{RV} the time in [s] between RV separation and predicted intercept. The time of RV separation for MRBMs with a 2,000 km range is around 2 minutes after launch, in accordance with the Iranian Emad missile

[21]. Furthermore, for BMs with a greater range and flight time, the moment of RV separation was scaled according to the latter. This approach yields a flight time before RV separation of up to 5 minutes for ICBM targets, which is in line with time frames for ICBM booster phases [22]. Note that for the target offset expression stated, the assumption is made that the PIP is based on one specific potential target's trajectory and not on the statistical expected target's trajectory, based on the cloud of potential targets.

Moreover, limited radar accuracy will also introduce an error which would be in the region of thousands of feet, depending on the radar (frequency band) used [23, p. 238]. This is short of enemy electronic warfare, denying radar measurements altogether. For this research, it is assumed that the the target offset introduced by errors in the radar measurements is 3000 ft or 914 m. However, lower frequency radars, like L-band[3] systems deployed on Royal Netherlands Navy frigates, are likely to introduce greater errors. Adopting the root sum square method to combine the two independent target offsets yields $o = \sqrt{25 \cdot t_{RV}^2 + 914^2}$.

2.3 U.S. Navy Ballistic Missile Defence Test (FTM-44)

In order to understand the implications of Vice Admiral Hill's statement mentioned in the introduction, it is important to investigate the BMD test on which he based his findings. Therefore, this section will elaborate further on the U.S. Navy BMD scenario FTM-44, conducted on November 16, 2020.

After the flight event, the MDA confirmed that the launch site of the ICBM dummy was Kwajalein, North Pacific. Apart from the launch site location, information on the test remains classified. However, on November 12, 2020, a navigational warning was issued for three specific areas in the Pacific [24]. The first area being the launch site itself. The other two are visualised in Figure 2.7. A number of planning parameters as to the performance of the target and interceptor missile can be estimated from these warning areas.

First, the ICBM dummy was most likely aimed at a location within the green area to prevent any safety hazards due to the FTM-44 test. This suggests that the ground range of the ICBM was slightly less than 6,800 km, the distance to the ICBM launch site from the entire eastern border of the area marked green. Moreover, the SM-3 launch and intercept site must have also been within the parameters of the green area because of the fact that the launcher had had to cut of its rocket stages. If performed outside the warning area this could have caused a dangerous situation.

Secondly, the yellow area appears to be the ICBM second rocket stage's drop site. If this is indeed a correct assumption, the ICBM dummy's trajectory was probably located above the full length of the yellow area. Extending the great circle line between the launch site and the yellow area all the way to the eastern border of the green area results in a ballistic trajectory somewhere between the orange lines drawn in Figure 2.7.

---

[3]1-2 GHz band.
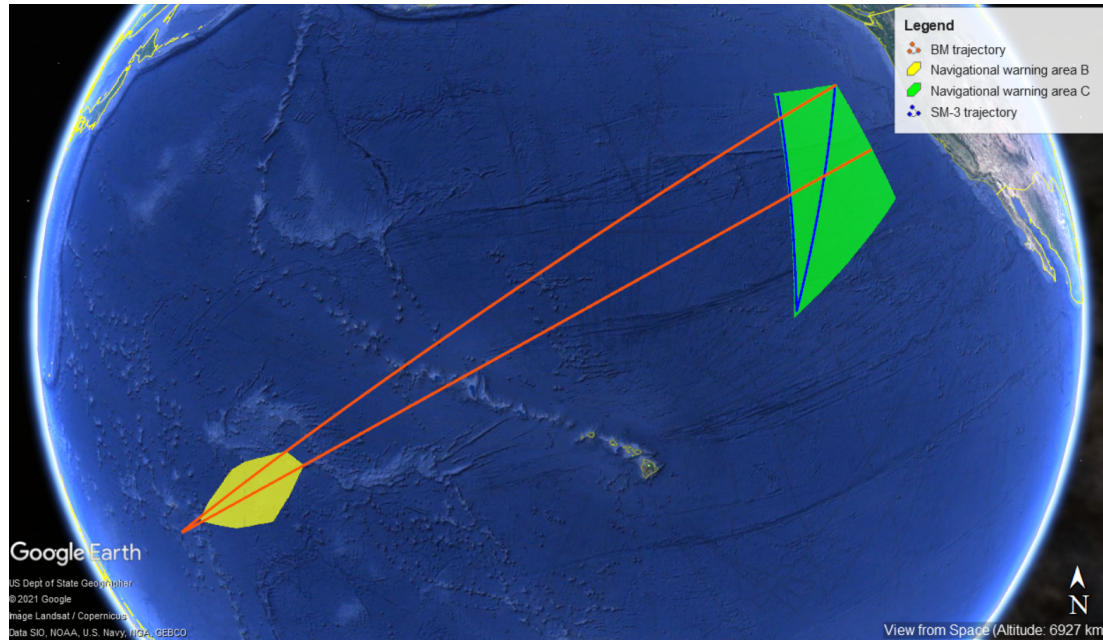
Figure 2.7: Navigational warning areas issued prior to FTM-44 BMD test.

Thirdly, assuming that the extended southwest corner of the green area was meant for launching the SM-3 and that the intercept took place somewhere on the ICBM flight path in the midwest part of the green area. The ground distance from the SM-3 launch site to the PIP must have been between 1,000 and 1,500 km. Also, the intercept would have taken place between 6,000 to 6,500 km from the launch site on Kwajalein. Furthermore, the SM-3's drop site with no intercept is likely to have been within the green area. This results in an SM-3 trajectory somewhere between the two blue lines in Figure 2.7 and a maximum SM-3 range of approximately 1,200 - 1,700 km. Assuming a minimum energy trajectory[4] for both missiles, the derived ranges correspond to ICBM and SM-3 burnout velocities of around 6.45 $\frac{km}{s}$ and 3.5 $\frac{km}{s}$, respectively.

Finally, to prevent space debris, the intercept must have taken place post-apogee for both ICBM and SM-3. Besides, according to Figure 1.3, the intercept took place near SM-3 apogee. Therefore, the intercept probably happened somewhat after the missile's apogee. The FTM-44 ballistic trajectories' parameters derived from the warning areas in Figure 2.7 are summed up in Table 2.2.

Table 2.2: Range of FTM-44 ballistic trajectories' parameters based on navigational warning areas and minimum energy trajectories.

Parameter	Lower limit	Upper limit	Adopted value
ICBM ground range [km]	6,400	6,800	6,644
ICBM ground range at intercept [km]	6,000	6,500	6,219
SM-3 ground range [km]	1,200	1,700	1,386
ICBM burnout velocity $[\frac{km}{s}]$	6.4	6.5	6.45
SM-3 burnout velocity $[\frac{km}{s}]$	3.3	3.8	3.5

---

[4]Trajectory that yields the greatest range for a given burnout velocity.

3. Methods

The following chapter aims to provide a clear description of the methods used to answer the research question. To do so, the Simulink® models will be described together with the simplifications and assumptions made by implementing these models. Secondly, several simulations that were ran using these models will be discussed.

3.1 Models

For this research, two models were used. These include a model that represents the BM's and SM-3's ballistic trajectories and a guidance model for the terminal phase. Both of the models were implemented in 2D and 3D. This section will focus on the 3D implementation. Nevertheless, it will be mentioned when simplifications apply for the 2D version.

3.1.1 Ballistic Trajectories

The ballistic trajectories of both missile and target were calculated in a Matlab® environment with code written by Savelsberg [25]. Moreover, the trajectories were based on the 2D closed-form solution of the equation of motion as stated by Zarchan [8, p. 245], which is the solution for a pure ballistic trajectory.

$$r(\theta) = \frac{r_0 \delta \cos^2(\gamma_0)}{1 - \cos(\theta) + \delta \cos(\gamma_0) \cos(\theta + \gamma_0)} \tag{3.1}$$

In Equation 3.1, r and θ indicate the position of the missile in a 2D Earth polar coordinate system in [rad] and [m], respectively. Additionally, r_0 and γ_0 are the missile's distance to the centre of the Earth in [m] and flight path angle (direction of velocity relative to the local horizontal) in [rad] at launch. Lastly, δ can be defined as follows:

$$\delta = \frac{r_0 V_{bo}^2}{GM_\oplus} \tag{3.2}$$

with V_{bo} the missile's burnout velocity in $[\frac{m}{s}]$ and $GM_\oplus$ the gravitational constant times Earth's mass (or Earth's standard gravitational parameter) in $[\frac{m^3}{s^2}]$.

The simplifcations made by applying Equation 3.1 are as follows:

- a perfectly round, non-rotating Earth;

- no aerodynamic forces act on either vehicle;

- at launch, both vehicles are given a velocity that is equal to V_{bo}, hereby neglecting the boost phase.

In the 2D model it was assumed that the target and interceptor were located in the same vertical plane.
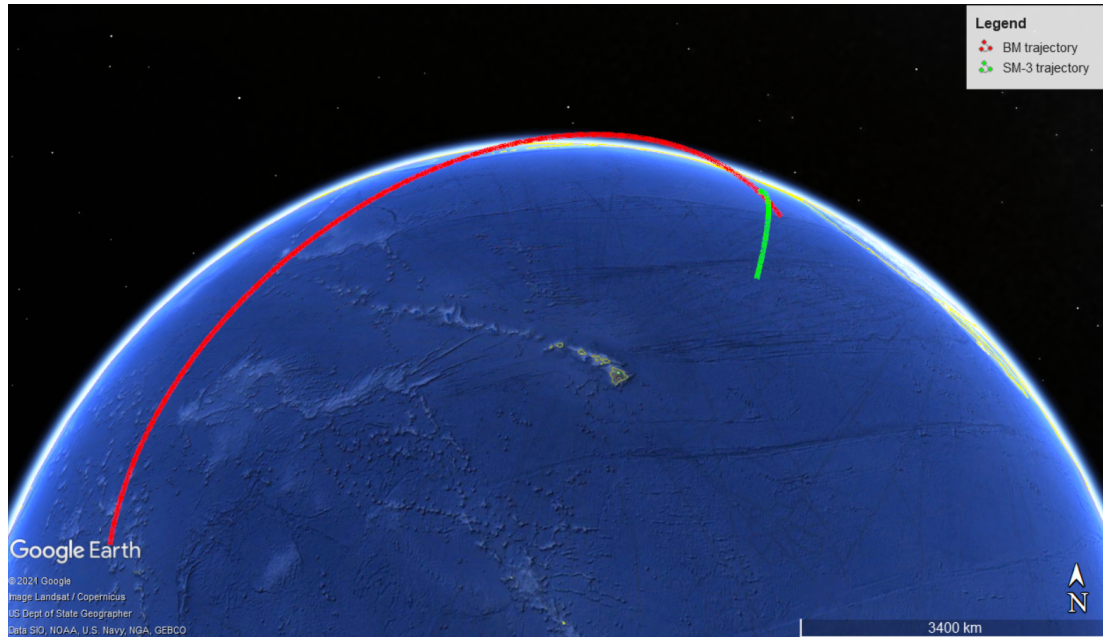
Figure 3.1: Estimate of FTM-44 ballistic trajectories.

The trajectories are largely located outside of the atmosphere, therefore neglecting any aerodynamic forces is a reasonable simplification. As for the other two simplifications mentioned, these will certainly change the outcome of the trajectories to some extent. However, the model should be sufficient for obtaining an idea on how the terminal phase intercept geometry looks like. Furthermore, when it comes to the KV's chances of success, this terminal phase is the critical part of the engagement. For these reasons, the adopted simplifications were considered reasonable for the model's purpose.

For a given ground range, two solutions for Equation 3.1 can be found (assuming a sufficient value for δ). These solutions are the lofted and depressed trajectories, for which the former will achieve a higher flight altitude than the latter. Besides, for a given V_{bo} the trajectory with the largest ground range is the so-called minimum energy trajectory. For this study, the target trajectories adopted were all minimum energy trajectories. Also, the interceptor missiles were all put on a depressed trajectory as this is often the fastest way to eliminate the target.

Moreover, firstly the model calculates the BM's minimum energy trajectory for a given $V_{bo,T}$ and launch site. Next, a PIP is selected for the interceptor to fly to. This PIP, together with the interceptor's launch site and $V_{bo,M}$ are then used to determine the interceptor's (depressed) ballistic trajectory. Hereafter, the 3D model generates a KML-file[1] of both trajectories for visualisation in Google Earth. An example of a BM trajectory, together with an interceptor trajectory can be seen in Figure 3.1.

3.1.2 Terminal Phase

The terminal phase starts after the interceptor travelled its ballistic trajectory and detects the target by means of the KV's IR seeker. To simulate the terminal phase and missile guidance, a Simulink® model was adopted based on proportional navigation. The

---

[1]Keyhole Markup Language file, used to visualise geographic content.

entire model is included in Appendices C.3 (2D) and C.4 (3D). Nevertheless, an overview of the guidance model is shown in Figure 3.2. Note that, even though the guidance models used for this study are written by the author, the 3D model was largely inspired by the work of Bos [7]. This section will further describe every submodel depicted in Figure 3.2. As well as introducing the coordinate systems used for the terminal phase.
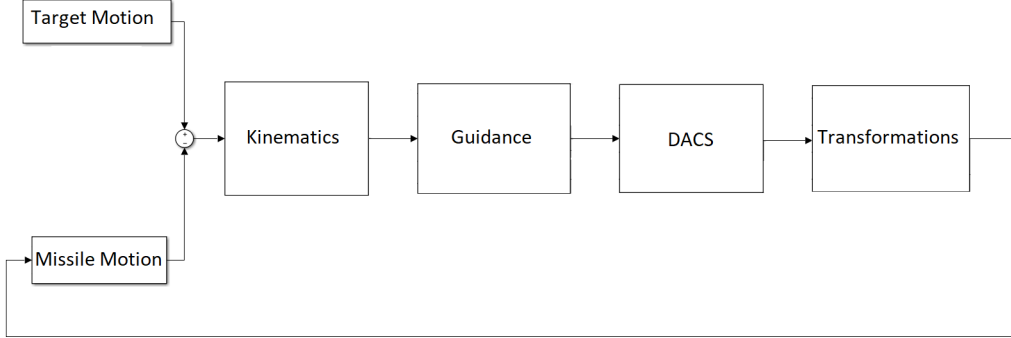
Figure 3.2: Guidance model overview.

Coordinate System

For the terminal phase, the coordinate systems were adopted as depicted in Figure 3.3. Both the 2D and 3D model use a coordinate system with the origin at the projection of the PIP on the Earth's surface. Since the 3D ballistic trajectories are derived in the Earth coordinate system, it is most convenient to use an East-North-Up local coordinate system (ENU) for 3D terminal phase simulations. A 2D engagement on the other hand, only includes the horizontal direction parallel to both target and interceptor trajectories. Also, the 2D ballistic trajectories were not generated relative to any Earth coordinate system. For these reasons, the use of cardinal directions was omitted in the 2D terminal phase coordinate system.

(a) 3D.   (b) 2D.
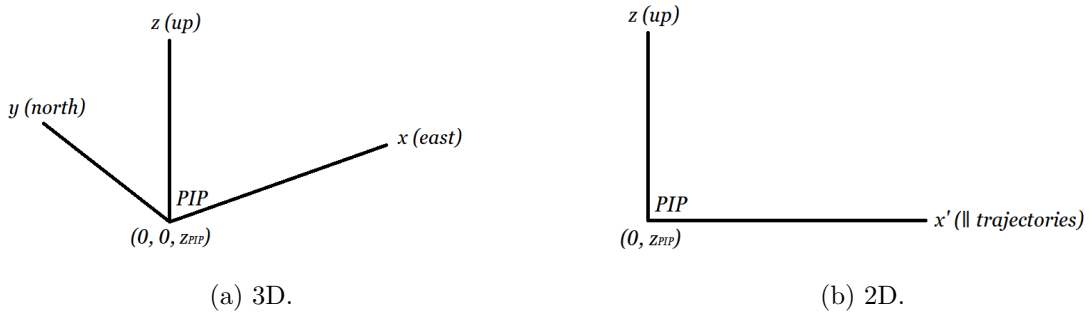
Figure 3.3: Coordinate systems adopted for the terminal phase.

Target and Missile Motion Submodels

The target and missile submodels numerically integrate the accelerations acting on the corresponding vehicles to solve for the vehicles' velocities and positions, respectively. The accelerations acting on the missile are those due to gravity and guidance. The target is only subject to gravity (neglecting any atmospheric residual). For both missile and target, the gravitational acceleration g in $[\frac{m}{s^2}]$ is of the same magnitude for a given

altitude and is directed in the local vertical direction (z):

$$g = -\frac{GM_{\oplus}}{(R_{\oplus} + z)^2} \tag{3.3}$$

with $R_{\oplus}$ representing the Earth's radius and z being the vehicle's current altitude both in [m]. Unlike the gravitational acceleration, the actual acceleration as a result of guidance has components in both x, y and z direction: $n_{a,x}$, $n_{a,y}$ and $n_{a,z}$. These values are required as input for the missile motion submodel.

Kinematics Submodel

After calculating the target's and missile's states at time t, the kinematics submodel uses these states to determine the:

- target-missile range R_{TM} in [m],

- closing velocity V_c in $[\frac{m}{s}]$,

- LOS in the horizontal direction λ_h in [rad],

- LOS in the vertical direction λ_v in [rad],

- the rate of LOS in the horizontal direction $\dot{\lambda}_h$ in $[\frac{rad}{s}]$ and

- the rate of LOS in the vertical direction $\dot{\lambda}_v$ in $[\frac{rad}{s}]$.

These six parameters are derived from Equations 3.4, 3.5, 3.6, 3.7, 3.8 and 3.9. The full derivations of V_c, $\dot{\lambda}_h$ and $\dot{\lambda}_v$ are included in Appendices A.2, A.3 and A.4, respectively.

$$R_{TM} = \sqrt{R_{TM_x}^2 + R_{TM_y}^2 + R_{TM_z}^2} \tag{3.4}$$

$$V_c = -\frac{R_{TM_x}V_{TM_x} + R_{TM_y}V_{TM_y} + R_{TM_z}V_{TM_z}}{R_{TM}} \tag{3.5}$$

$$\lambda_h = \arctan\left(\frac{R_{TM_y}}{R_{TM_x}}\right) \tag{3.6}$$

$$\lambda_v = \arctan\left(\frac{R_{TM_z}}{\sqrt{R_{TM_x}^2 + R_{TM_y}^2}}\right) \tag{3.7}$$

$$\dot{\lambda}_h = \frac{R_{TM_x}V_{TM_y} - R_{TM_y}V_{TM_x}}{R_{TM_x}^2 + R_{TM_y}^2} \tag{3.8}$$

$$\dot{\lambda}_v = \frac{(R_{TM_x}^2 + R_{TM_y}^2)V_{TM_z} - R_{TM_z}(R_{TM_x}V_{TM_x} + R_{TM_y}V_{TM_y})}{(R_{TM_x}^2 + R_{TM_y}^2 + R_{TM_z}^2)\sqrt{R_{TM_x}^2 + R_{TM_y}^2}} \tag{3.9}$$

R_{TM_x}, R_{TM_y} and R_{TM_z} represent the distance between target and missile in [m] in the x-, y- and z-direction, respectively. Moreover, V_{TM_x}, V_{TM_y} and V_{TM_z} denote the relative velocity between target and missile in $[\frac{m}{s}]$ in the x-, y- and z-direction. Note that for a 2D intercept geometry, Equations 3.6 and 3.8 can be omitted and that λ_v and $\dot{\lambda}_v$ in Equations 3.7 and 3.9 become λ and $\dot{\lambda}$, respectively. Also, Equations 3.4, 3.5, 3.7 and 3.9 can be simplified by leaving out the R_{TM_y} and V_{TM_y} terms.

Besides, in the kinematics submodel a stop condition was implemented for $V_c < 0$ to end the simulation, as this means that target and missile have had their closest point of approach (being either an intercept or a certain miss distance).

Guidance Submodel

The results of Equations 3.6 and 3.7, together with N are then used to calculate the demanded accelerations $n_{d,h}$ and $n_{d,v}$ in $[\frac{m}{s^2}]$, perpendicular to λ_h and λ_v, respectively. This is done according to Equations 2.2 and 2.3. However, for the 2D model these equations reduce to Equation 2.1.

Additionally, in the guidance submodel a constraint is built in that the missile guidance only starts after t_{ID} seconds after the start of the engagement. This way, the time needed for proper target identification and tracking was taken into account.

DACS Submodel

Hereafter, $n_{d,h}$ and $n_{d,v}$ are used as input for a first order system. Hereby, a time delay is introduced for the KV system as a whole, which includes time needed for:

- gathering sufficient track data;

- the flight control system to convert track data into acceleration demands and

- achieving the maximum acceleration.

For this research a time constant of $Tc = 0.5$ s was adopted[2]. However, since the KV applies the greatest divert right after target acquisition, it does so at a moment at which there is still sufficient time. Therefore, the precise value of Tc should not impact the adequacy in which the model approaches the guidance problem. The output of the first order system is then subject to a saturation block, which indicates the maximum acceleration that the DACS can generate. Besides, only a maximum ΔV is allowed, taking into account the finite amount of propellant. The result of these transformations is the actual lateral acceleration due to guidance $n_{a,h}$ and $n_{a,v}$ perpendicular to λ_h and λ_v, respectively.

Transformations Submodel

The values for $n_{a,h}$ and $n_{a,v}$ are then transformed from the horizontal and vertical direction into the x, y and z directions via Equations 3.10, 3.11 and 3.12.

$$n_{a,x} = -n_{a,h}\sin(\lambda_h) - n_{a,v}\sin(\lambda_v)\cos(\lambda_h) \tag{3.10}$$

$$n_{a,y} = n_{a,h}\cos(\lambda_h) - n_{a,v}\sin(\lambda_v)\sin(\lambda_h) \tag{3.11}$$

$$n_{a,z} = n_{a,v}\cos(\lambda_v) \tag{3.12}$$

For the 2D model, these equations can be simplified as follows.

$$n_{a,x'} = -n_a\sin(\lambda) \tag{3.13}$$

$$n_{a,z} = n_a\cos(\lambda) \tag{3.14}$$

The values for $n_{a,x}$, $n_{a,y}$ and $n_{a,z}$ are then used as input for the missile motion submodel.

---

[2]In 0.5 s 63% of the maximum (difference in) lateral acceleration is achieved.

Initial Conditions

For all of this to work, the model needs the correct initial conditions for both vehicles. These include x_0-, y_0 and z_0-coordinates and the velocity components $V_{0,x}$, $V_{0,y}$ and $V_{0,z}$.

For the terminal phase model, the same simplifications were adopted as described in Section 3.1.1, except in this model, the Earth was assumed to be flat. Since the distances covered during the terminal phase are relatively small, this is considered a reasonable simplification. However, due to the difference in approach between the terminal phase guidance model and the ballistic trajectories model, their results in vehicle dynamics were slightly different as well. This resulted in a miss without there being any target offset as the guidance model was implemented from a certain point on the ballistic trajectory on. To prevent this systematic error from occurring, the terminal phase model itself was used to calculate the target and missile dynamics reversed in time from the PIP in the ballistic trajectories model to an R_{TM} at which target detection was considered possible R_{IR}. Since the same model was used for calculating these reversed trajectories, as for the actual terminal phase, any error was eliminated. This approach was adopted from research by Bos [7]. Furthermore, the Matlab® scripts used for calculating the reversed trajectories in 2D and 3D are included in Appendices C.1 and C.2.

3.2 Simulations

This section will describe the simulations that were conducted in order to gather results from the models discussed in the Section 3.1. For most of the research, the 2D model was adopted for simplicity reasons. Only for investigating the FTM-44 flight event a 3D approach was deemed necessary. Therefore, this section will start with a justification of the 2D approach. The remainder of this section is divided into three subsections that represent three different BM intercept scenarios, which are also illustrated in the road map in Figure 3.4. In this figure, every rectangle stands for certain information and every ellipse indicates a simulation or a set of simulations.

3.2.1 Justification of the 2D Approach

Performing simulations in two dimensions rather than three yields one major advantage in particular. According to Bos [7] three dimensional analysis of the terminal phase makes isolating the effects of various parameters rather complex. It makes it hard to comprehend what is going on in certain BM engagement scenarios. Adopting a 2D approach instead can help clarify relationships between intercept parameters. Yet it is important to substantiate the validity of a 2D intercept geometry.

The first major simplification in the 2D approach is leaving out the target offset in the horizontal direction perpendicular to x'. However, in Section 2.1.1 it is explained that the demanded lateral acceleration in 3D is nothing more than the 2D equivalent, but with one extra direction of interest, the one perpendicular to λ_h. This is exactly the lateral acceleration needed to countervail the additional offset introduced in 3D. Besides, in Section 2.1.2 it became clear that for a 3D geometry, an additional pair of nozzles with their own capabilities is introduced to generate this lateral acceleration. Therefore, when considering a 3D approach, there are actually two separate 2D BM engagements: an extra target offset, requiring additional lateral acceleration and an extra pair of DCS nozzles to generate this acceleration.
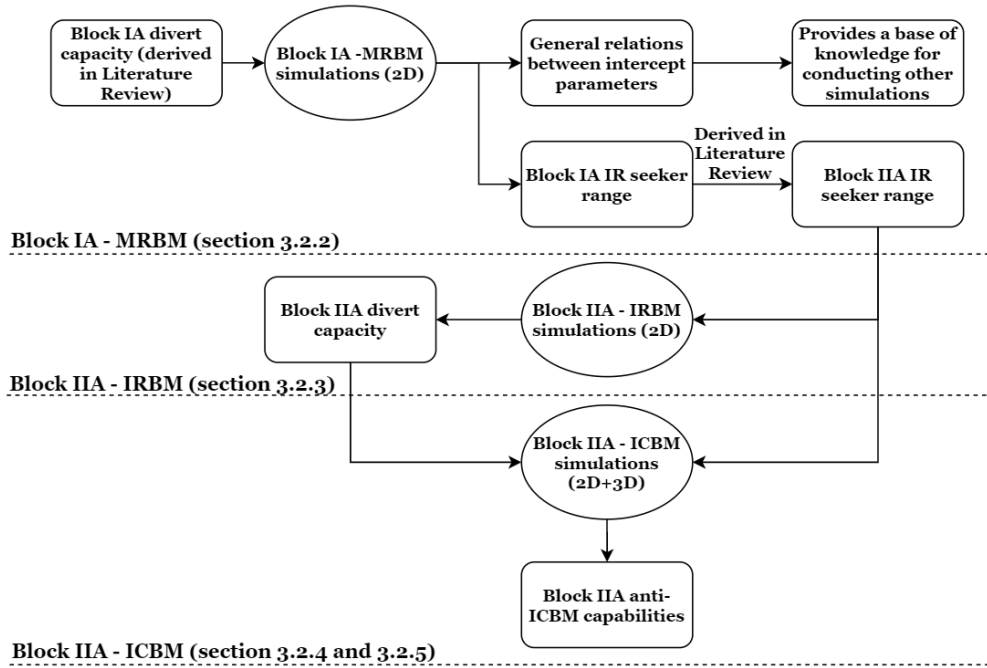
Figure 3.4: Simulations road map.

The second difference addressed is that of the relative flight path angle, which is the angle in which KV and RV approach each other. Since in 3D this angle has an extra component in the horizontal plane, it is hard to compare 2D and 3D. However, the closing velocity and therefore the time the KV has to perform a divert, can just as well be simulated in 2D. Besides, this study will often use the most pressing intercept geometry to derive the results from, which will prove to be a head-on engagement. This intercept geometry is just as well simulated using a 2D model as it is with a 3D model.

Nevertheless, after deriving the specifications required for the Block IIA KV to live up to the capabilities claimed by the manufacturer, the 3D implementation was used to simulate the FTM-44 and other ICBM intercept geometries. This 3D approach was deemed necessary because the combination of relative flight path angle and closing velocity that occurred in the FTM-44 test is not convertible to a 2D engagement.

3.2.2 Block IA MRBM Interceptions

To understand the FTM-44 test, it is necessary to start with what is already known. Since most specifications of the SM-3 Block IA KV were derived in the Literature Review section, the first set of simulations conducted were also Block IA intercept scenarios. This way, it was possible to obtain a general idea of the coherence between different intercept parameters. These parameters include target offset, flight path angles, closing velocity, IR seeker range, total divert and lateral acceleration. The only parameter that has not been considered yet, is the Block IA burnout velocity. Therefore, it is assumed to be $V_{bo,M} = 3 \ \frac{\text{km}}{\text{s}}$ according to existing literature. Moreover, the intercept scenario that was used is visualised in Figure 3.5.
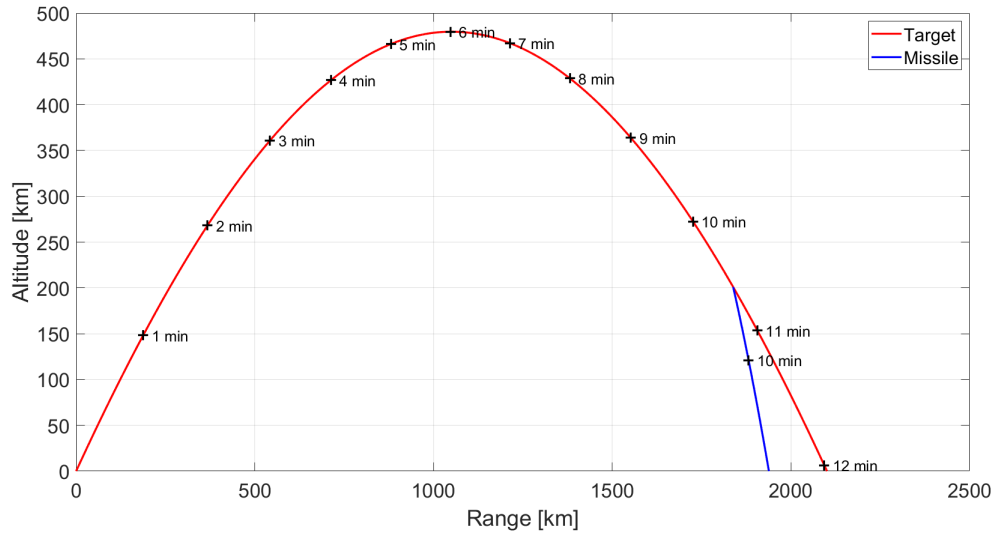
Figure 3.5: Example of an SM-3 Block IA MRBM intercept geometry (for a ground
distance PIP to SM-3 launch site of 100 km).

The parameter values adopted in these simulations are as follows (unless stated otherwise):

- BM ground range of 2,101 km;

- PIP altitude of 200 km;

- IR seeker range $R_{IR} = 100$ km;

- effective navigation ratio $N = 3$;

- KV first order system time constant $T_c = 0.5$ s;

- time needed for target identification and tracking $t_{ID} = 2$ s;

- target burnout velocity $V_{bo,T} = 4.2 \ \frac{\text{km}}{\text{s}}$;

- missile burnout velocity $V_{bo,M} = 3 \ \frac{\text{km}}{\text{s}}$.

Target Offset

To obtain a general understanding of what the target offset does to the n_a and ΔV, the
models described were run for different offsets $o_{x'}$ and o_z. The ΔV and n_a for every
offset were then plotted as a contour in the $o_{x'}$ - o_z plane. This process was repeated
for different intercept geometries. For this, the parameter values were used as listed
above. Note that the IR seeker range adopted is completely arbitrary, but this should
not matter in the sense of finding out the target offset's effect on the divert capacity in
a qualitative context. For this simulation, no restrictions were laid upon the n_a and ΔV
the DACS is able to generate. Hence, the only difference between n_d and n_a was a time
delay introduced by the first order flight control system. The results of this simulation
will be elaborated upon in the Results Section 4.1.1.

Relative Flight Path Angle γ_{TM} and Closing Velocity V_c

After concluding that only the target offset perpendicular to λ_p ($o_{\perp\lambda_p}$) affects the divert, it was possible to only use $o_{\perp\lambda_p}$ to parametrize the offset. In the next simulation, the effects of the relative flight path angle γ_{TM} and the closing velocity V_c on the maximum lateral acceleration and total divert were investigated. To do so, the SM-3 launch site was shifted from 500 km in front of the PIP to 500 km behind the PIP (ground distance). This was done for different target offsets $o_{\perp\lambda_p}$. After the simulation, ΔV and n_a were plotted as a contour on the γ_{TM} - $o_{\perp\lambda_p}$ and V_c - $o_{\perp\lambda_p}$ planes. These results are displayed in the Results Section 4.1.2.

IR Seeker Range R_{IR}

Next, a similar simulation to the one described in the previous section was conducted to find the coherence between the IR seeker's range and the lateral acceleration and total divert. The models described were run for different target offsets perpendicular to λ_p and different IR ranges. The lateral acceleration and total divert were then plotted as a function of the IR capabilities and target offset. For this simulation, the same parameters were used as in the previous section (however in this simulation R_{IR} is a variable). Moreover, a relative flight path angle of 180° (ground distance PIP to launch site SM-3 of 240 km) was adopted, as this proved to be the most pressing case in the previous simulation.

As stated in Section 2.1.3, the value for the seeker's NEFD is yet to be determined. To estimate the NEFD, SM-3 Block IA engagements with different intercept geometries were simulated. For this, the SM-3 launch site was again shifted over a ground distance of 1,000 km from 500 km in front of the PIP to 500 km behind the PIP. The NEFD required for a target kill regardless of the SM-3 launch site was then considered the SM-3 Block IA seeker's sensitivity. Lastly, a comparison was made between this value and the NEFD parameter space in Section 2.1.3 for validation. For the simulation described, the following (additional) parameters were adopted:

- maximum $\Delta V = 274.7 \frac{m}{s}$ and maximum $n_a = 23.1 \frac{m}{s^2}$ (see Section 2.1.2);

- target offset of 2,709 m perpendicular to λ_p (in accordance with Section 2.2).

After finding the Block IA sensor's NEFD, a Block IIA NEFD of 2.5 times smaller was adopted, in accordance with Section 2.1.3. The results of the simulations regarding R_{IR} will be elaborated upon in the Results Section 4.1.3.

3.2.3 Block IIA IRBM Interceptions

The next simulation involved a Block IIA 2D intercept geometry. The ballistic trajectories of that geometry are visualised in Figure 3.6.
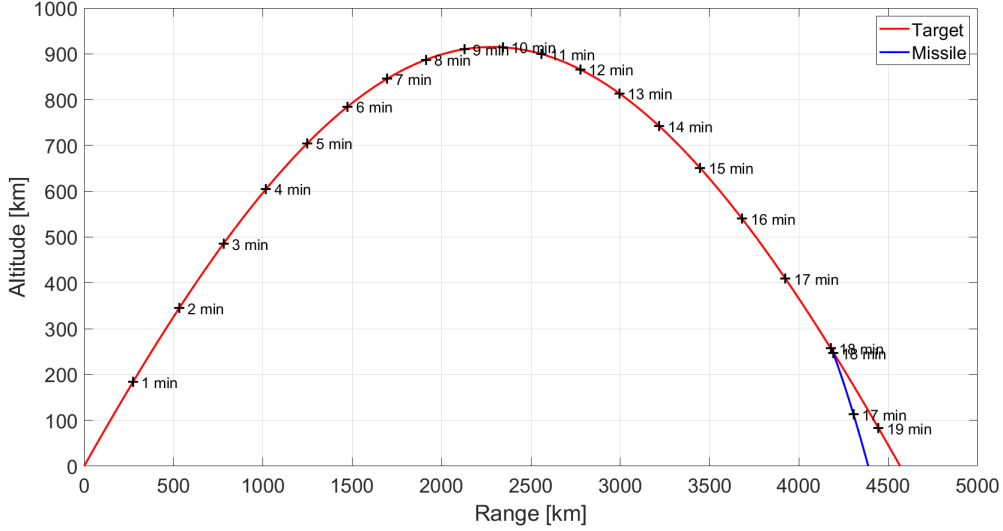
Figure 3.6: Example of an SM-3 Block IIA IRBM intercept geometry (for a ground
distance PIP to SM-3 launch site of 200 km).

Moreover, the parameters used for this simulation are as follows:

- BM ground range of 4,566 km;

- PIP altitude of 250 km;

- effective navigation ratio $N = 3$;

- KV first order system time constant $T_c = 0.5$ s;

- time needed for target identification and tracking $t_{ID} = 2$ s;

- target burnout velocity $V_{bo,T} = 5.7 \, \frac{\text{km}}{\text{s}}$;

- missile burnout velocity $V_{bo,M} = 3.5 \, \frac{\text{km}}{\text{s}}$;

- IR seeker range $R_{IR} = 171$ km, according to the findings from the previous section;

- target offset of 4,518 m perpendicular to λ_p (in accordance with Section 2.2).

Block IIA Divert Capacity

After estimating the Block IIA IR range based on the simulations described in Section
3.2.2, it was possible to put a constraint on the divert capacity (ΔV and n_a) that is
needed for the tasks the Block IIA was made for. Those are head-on ($\gamma_{TM} = 180°$) IRBM
interceptions. For this, a simulation was conducted to determine the miss distance for
different values of ΔV and n_a available. These miss distances were then plotted in the
ΔV - n_a plane. The combinations that caused a miss distance of 0.1 m or smaller were
then considered sufficient for an intercept. Next, the lower values for the divert capacity
to cause a hit were accepted as the Block IIA divert capacity. Note that the ways in
which the Block IIA TDACS and Block IA SDACS operate are different as explained
in Section 2.1.2. However, since the TDACS operation method is not fully known, for
this research, the TDACS is assumed an SDACS equivalent with greater divert capacity.
The results of this simulation will be displayed in the Results Section 4.2.1.

3.2.4 Block IIA ICBM Interceptions 2D

After gathering all the Block IIA specifications, the missile was put to the test by simulating ICBM interceptions. For this, the ballistic trajectories were adopted as depicted in Figure 3.7.
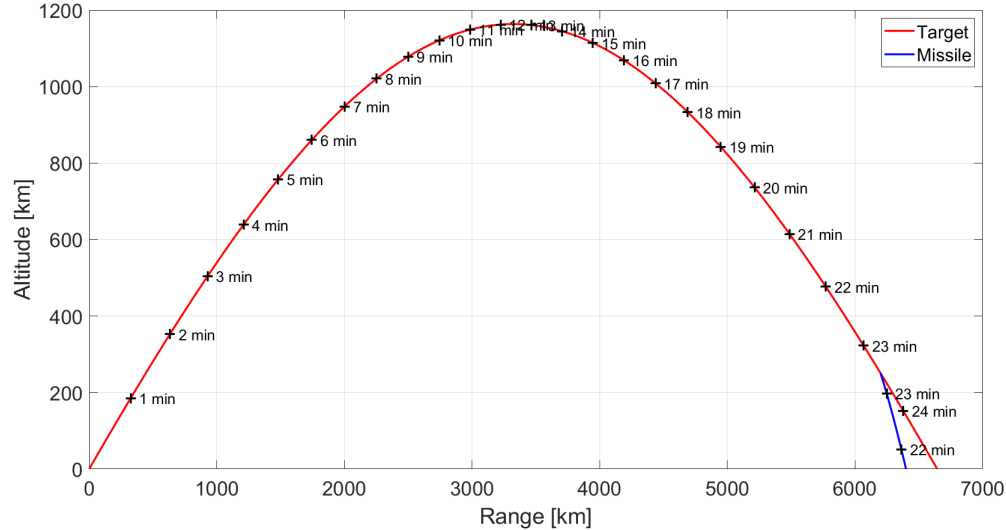

Figure 3.7: Example of an SM-3 Block IIA ICBM intercept geometry (for a ground distance PIP to SM-3 launch site of 200 km).

The intercept parameters that correspond to Figure 3.7 are as follows:

- BM ground range of 6,644 km;

- PIP altitude of 250 km;

- effective navigation ratio $N = 3$;

- KV first order system time constant $T_c = 0.5$ s;

- time needed for target identification and tracking $t_{ID} = 2$ s;

- target burnout velocity $V_{bo,T} = 6.45 \ \frac{\text{km}}{\text{s}}$;

- missile burnout velocity $V_{bo,M} = 3.5 \ \frac{\text{km}}{\text{s}}$;

- IR seeker range $R_{IR} = 104$ km, according to earlier findings;

- target offset of 5,877 m perpendicular to λ_p (in accordance with Section 2.2);

- maximum $\Delta V = 360 \ \frac{\text{m}}{\text{s}}$ and maximum $n_a = 30 \ \frac{\text{m}}{\text{s}^2}$, according to findings from the previous simulation.

Relative Flight Path Angle γ_{TM} and Closing Velocity V_c

First, the effect of γ_{TM} on the miss distance was investigated. For this, the SM-3 launch site was shifted over a ground distance of 2,000 km from 1,000 km in front of the PIP to 1,000 km behind the PIP. Hereafter, the miss distances were plotted against the SM-3 launch site and relative flight path angle γ_{TM}. Secondly, the same curves were generated for V_c instead of γ_{TM}. The results of this simulation can be seen in the Results Section 4.3.1.

Target Range

Secondly, a 2D simulation was executed in which different kinds of ICBM targets were engaged. For this, a set of ICBM targets was adopted on a minimum energy trajectory with a $V_{bo,T}$ ranging from 6.2 to 7.5 $\frac{km}{s}$ (see Figure 3.8). The SM-3 launch sites were all chosen in a way that the value for γ_{TM} remained fairly constant for every intercept, that is between 28° and 38°. Moreover, for every intercept a target offset was adopted in accordance with Section 2.2 and the PIP altitude was kept constant at 250 km. For every ICBM range, the miss distance was plotted in order to gain insight in what kind of targets the Block IIA's KV can negate.
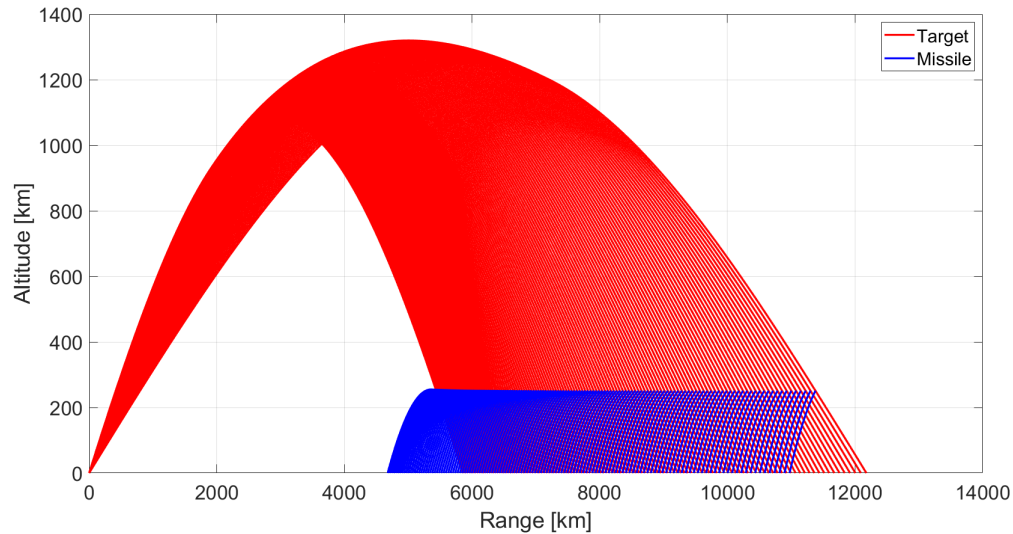

Figure 3.8: Ballistic ICBM and interceptor trajectories.

Next, in order to find out what part of a certain miss distance is introduced by an increase in target offset and what part by a greater V_c, both graphs of the miss distances for constant target offset and that for a constant V_c were also included in the Results Section 4.3.2.

3.2.5 Block IIA ICBM Interceptions 3D

Finally, several ICBM engagements were simulated in 3D using the Block IIA IR range and divert capabilities as derived from the 2D simulations. As a starting point, the estimate of the FTM-44 intercept geometry in Figure 3.1 was used. The intercept parameters adopted for these simulations are as follows:

- ICBM launch site 9.005°N 167.728°E (Kwajalein);

- BM ground range of 6,644 km;

- PIP altitude of 250 km;

- Effective navigation ratio $N = 3$;

- KV first order system time constant $T_c = 0.5$ s;

- time needed for target identification and tracking $t_{ID} = 2$ s;

- target burnout velocity $V_{bo,T} = 6.45 \; \frac{\text{km}}{\text{s}}$;

- missile burnout velocity $V_{bo,M} = 3.5 \; \frac{\text{km}}{\text{s}}$;

- IR seeker range $R_{IR} = 104$ km, according to findings from the 2D simulations;

- target offset of 5,877 m perpendicular to $\lambda_{v,p}$ and 5,877 m perpendicular to $\lambda_{h,p}$ (in accordance with Section 2.2);

- maximum $\Delta V = 360 \; \frac{\text{m}}{\text{s}}$ and maximum $n_a = 30 \; \frac{\text{m}}{\text{s}^2}$, according to findings from the 2D simulations.

FTM-44

Firstly, a simulation was conducted of the FTM-44 flight event assuming the parameters in the final column of Table 2.2 and the trajectories in Figure 3.1. From this simulation, a couple of intercept parameters were derived and depicted in appropriate figures. These figures are included in the Results Section 4.4.1.

SM-3 Launch Site in the FTM-44 BMD Test

Secondly, a set of simulations was conducted in which different SM-3 launch sites were adopted. These SM-3 launch sites were distributed in a circle centred around the projection of the PIP on the ground with a radius of 9.5 degrees of latitude/longitude. After the simulation, a contour plot was generated that shows for every SM-3 launch site to yield either a miss or a hit. Also, the estimated FTM-44 SM-3 launch site was indicated in this plot, which can be seen in the Results Section 4.4.2.

IR Range, Target Offset and PIP in the FTM-44 BMD Test

Lastly, in order to investigate the effects of the target's IR signature and offset on the outcome of the FTM-44 scenario, a simulation was conducted with different IR ranges and target offsets. Again, the parameter hit or miss for every target offset was plotted and a region of feasible combinations of the two parameters was established that would have resulted in an intercept during the actual BMD test. The same procedure was followed for a combination between IR range and PIP altitude. The results of this final simulation are included in the Results Section 4.4.3.

4. Results and Discussion

In this chapter the results that follow from the simulations described in the Methods Section 3.2 will be displayed and elaborated upon.

4.1 Block IA MRBM Interceptions

4.1.1 Target Offset

Figure 4.1 shows a ballistic intercept geometry, together with two contour plots indicating the ΔV and maximum n_a adopted by the KV for a certain target offset $o_{x'}$ and o_z. Also, the predicted LOS direction λ_p has been added to the figure. From Figure 4.1 it can be derived that it is only the target offset perpendicular to λ_p that affects the divert that the KV applies. This is confirmed by the results for other intercept geometries, which are included in Appendix B.1.

(a) Ballistic trajectories.

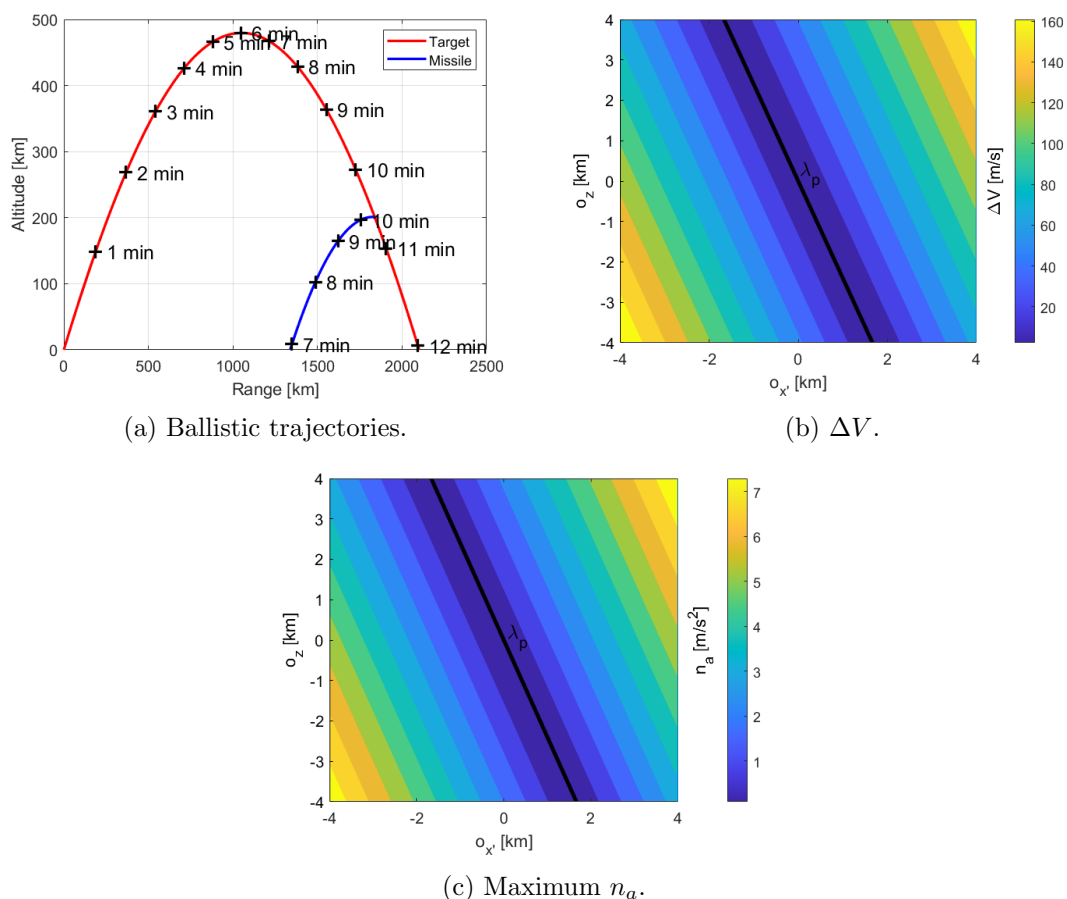
(b) ΔV.

(c) Maximum n_a.

Figure 4.1: ΔV and maximum n_a as a function of target offset for a ground distance PIP to launch site SM-3 of -500 km.

4.1.2 Relative Flight Path Angle γ_{TM} and Closing Velocity V_c

Figure 4.2 (a) and (b) show the impact of γ_{TM} on the total divert and maximum lateral acceleration, respectively. From this contour plot it becomes clear that a head-on engagement ($\gamma_{TM} = 180°$) yields the most challenging case for the KV. Both the total divert and the maximum acceleration peak for this intercept geometry. For a doubling of the target offset, the adopted ΔV and n_a become twice as big (as indicated by the data tips).
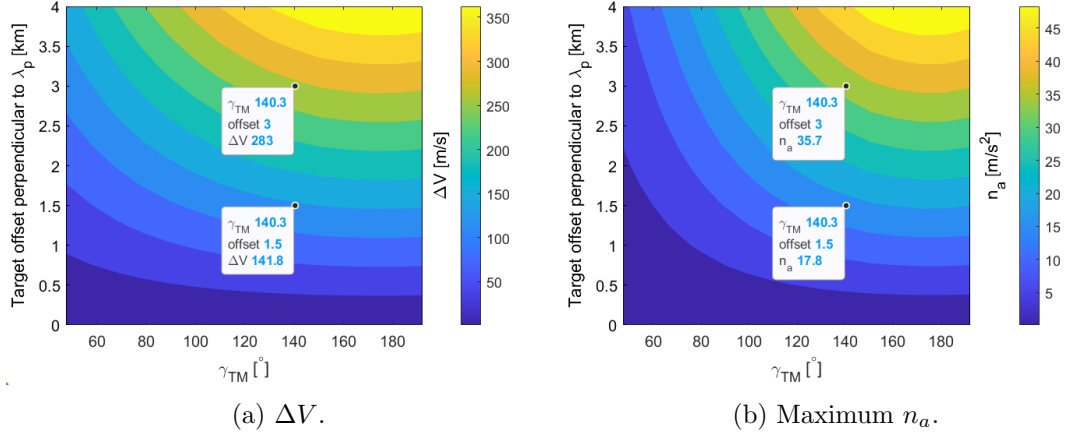

(a) ΔV.   (b) Maximum n_a.

Figure 4.2: ΔV and maximum n_a as a function of target offset $o_{\perp\lambda_p}$ and γ_{TM} ($R_{IR} = 100$ km).

Figure 4.3 (a) and (b) show the impact of V_c on the total divert and maximum acceleration. What stands out in these graphs is that (a) and (b) do not have exactly the same shape. This can be explained by the fact that a relatively small closing velocity yields more time for the KV to adjust its course. Therefore, the KV has more time to implement the ΔV and requires a much smaller lateral acceleration. The total divert however, is the lateral acceleration integrated over time and is therefore much less affected by the greater closing velocity. This phenomenon can also be observed in Figure 4.2 and the results in the next section.
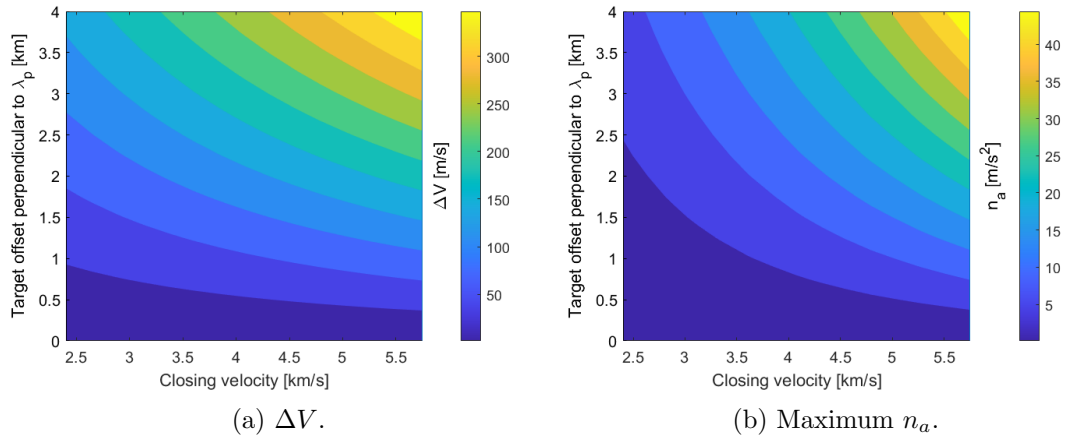

(a) ΔV.   (b) Maximum n_a.

Figure 4.3: ΔV and maximum n_a as a function of target offset $o_{\perp\lambda_p}$ and V_c ($R_{IR} = 100$ km).

4.1.3 IR Seeker Range R_{IR}

Figure 4.4 (a) and (b) show the impact of the IR seeker range on the total divert and maximum lateral acceleration, respectively. Similar to the results indicating the influence of V_c in the previous section, the R_{IR} affects the time available for the KV to adjust its course. Therefore, a greater R_{IR} causes the KV to produce a smaller ΔV and n_a in order to ensure a target intercept.
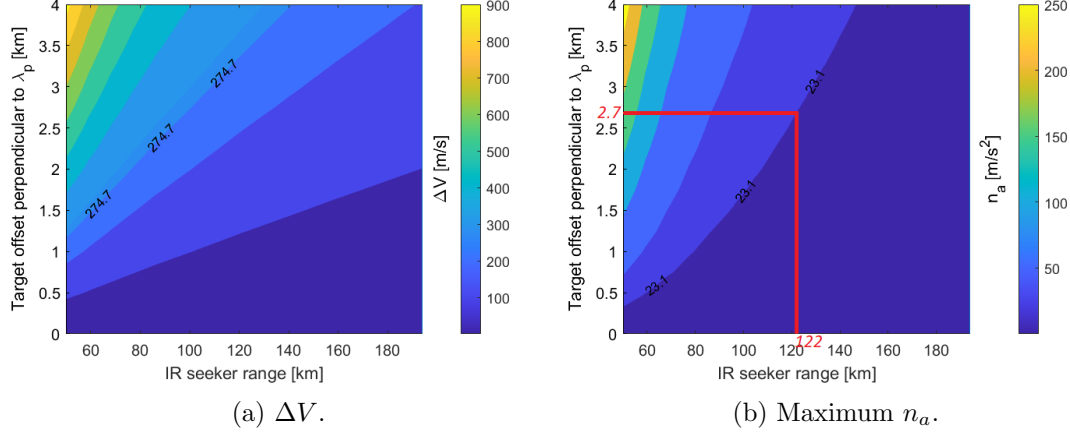

(a) ΔV.   (b) Maximum n_a.

Figure 4.4: ΔV and maximum n_a as a function of target offset $o_{\perp \lambda_p}$ and R_{IR} ($\gamma_{TM} = 180°$).

Assuming a maximum target offset of $o_{\perp \lambda_p} = 2{,}709$ m, Figure 4.4 (b) yields a required R_{IR} of ≈ 122 km based on the constraint on the maximum lateral acceleration of $n_a = 23.1 \frac{\text{m}}{\text{s}^2}$. However, Figure 4.5 (a) proves an IR range of 108 km to be sufficient for the same geometry, target offset and divert capacity. This is due to the fact that the peak acceleration demanded by the KV is not actually needed, as a somewhat smaller n_a for a longer period of time also suffices for a target hit (see Figure 4.5 (b)).
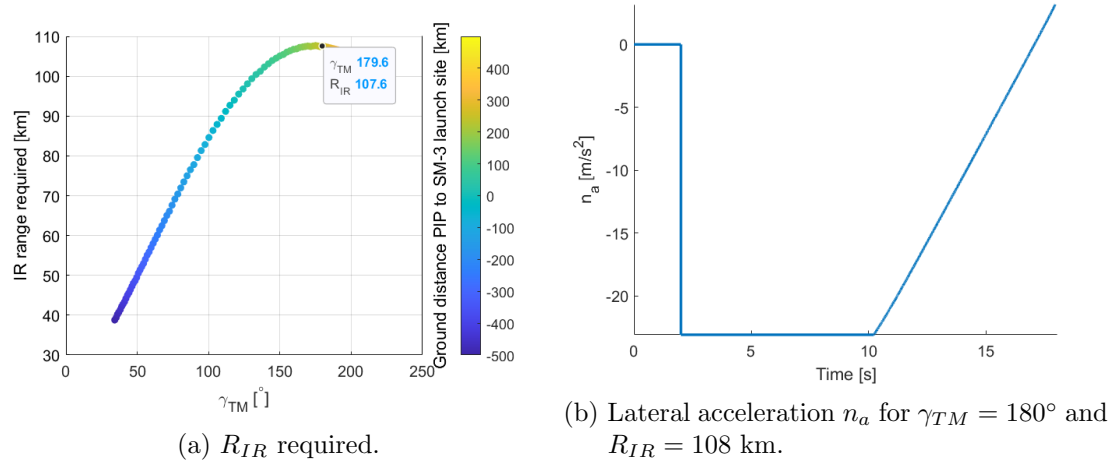

(a) R_{IR} required.

(b) Lateral acceleration n_a for $\gamma_{TM} = 180°$ and $R_{IR} = 108$ km.

Figure 4.5: IR range required for Block IA MRBM intercept ($o_{\perp \lambda_p} = 2{,}709$ m).

For an IR range required of 108 km, the Block IA seeker needs to have an NEFD of $5 \cdot 10^{-10} \frac{\text{W}}{\text{m}^2}$. This yields a Block IIA NEFD of $\frac{5 \cdot 10^{-10}}{2.5} \approx 2 \cdot 10^{-10} \frac{\text{W}}{\text{m}^2}$. Moreover, the lower bound Block IIA IR range would be $\sqrt{2.5} \cdot 108 \approx 171$ km for MRBM/IRBM threats and $\frac{1.47 \cdot 10^{-3}}{\sqrt{2 \cdot 10^{-10}}} \approx 104$ km for ICBM targets (in accordance with Section 2.1.3). Note that

both of the values found for the NEFD lie well within the parameter space defined in Section 2.1.3.

4.2 Block IIA IRBM Interceptions

4.2.1 Block IIA Divert Capacity

Figure 4.6 shows the miss distance in the Block IIA IRBM engagement for different values of ΔV and n_a available. Note that the scenario in this simulation is one that the Block IIA is able to handle in reality. Therefore, the divert capacity of the DACS should be sufficient for a hit. A set of feasible combinations of ΔV and n_a can be derived from this figure. This set includes the combinations that lie in the upper right corner of the contour plot. One of the lower values for the divert capacity being sufficient for a hit is indicated by the data tip: $\Delta V = 360 \ \frac{m}{s}$, $n_a = 30 \ \frac{m}{s^2}$. These are the values adopted for the remaining Block IIA simulations.
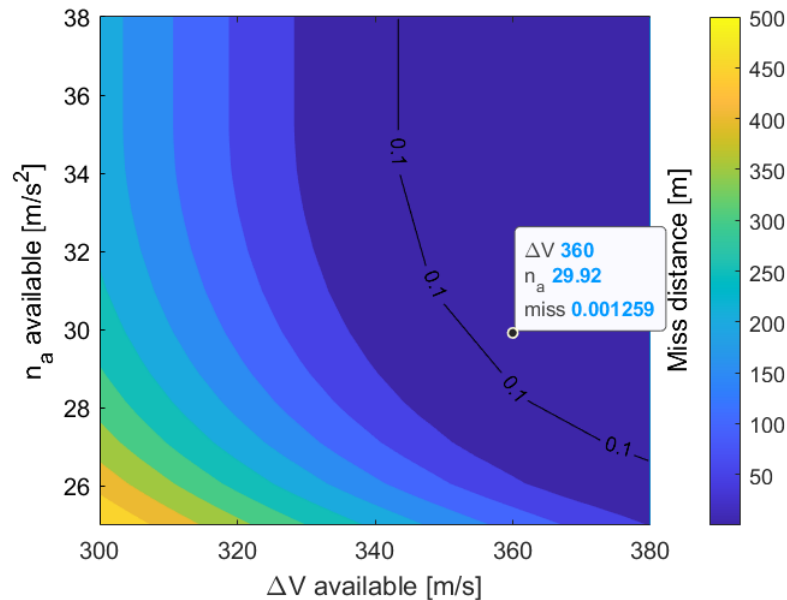

Figure 4.6: Miss distance as a function of ΔV and n_a available.

4.3 Block IIA ICBM Interceptions 2D

4.3.1 Relative Flight Path Angle γ_{TM} and Closing Velocity V_c

Figure 4.7 shows the miss distance for different ICBM intercept geometries, adopting a divert capacity and IR seeker range as derived in the prior simulations. The data tip reveals that the maximum relative flight path angle γ_{TM} for an intercept is $33°$. Again, the head-on engagement proves to yield the most challenging situation for the KV.
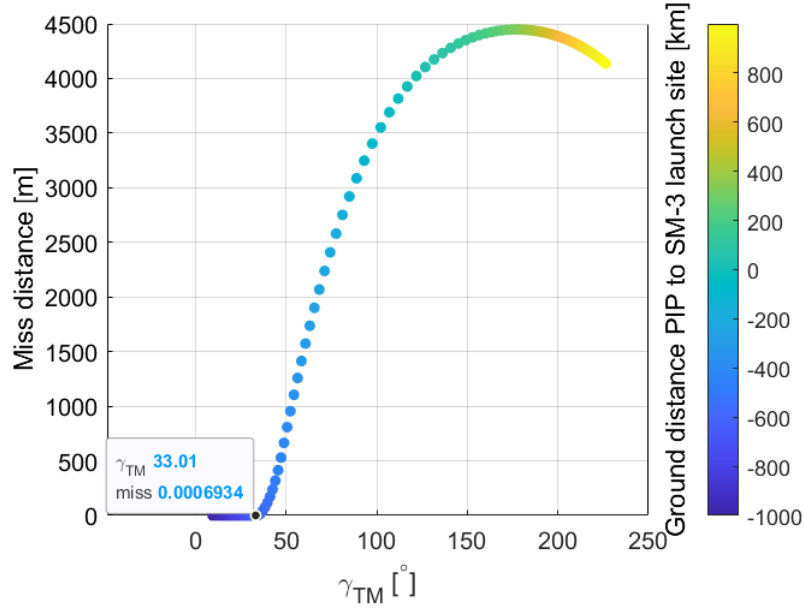
Figure 4.7: Miss distance as a function of γ_{TM}.

Figure 4.8 shows the miss distance for the different closing velocities that follow from shifting the SM-3 launch site. From the figure it can be derived that the maximum closing velocity for an intercept is 3.94 $\frac{km}{s}$. However, 3.94 $\frac{km}{s}$ is less than the closing velocity one can expect in an IRBM head-on engagement. This can be explained by the greater target offsets and smaller IR ranges that occur during ICBM interceptions. The effect of target offset will be further evaluated upon in the next section. Figure 4.7 and 4.8 illustrate that, under the right circumstances, the Block IIA is capable of intercepting the ICBM target used in the simulation.
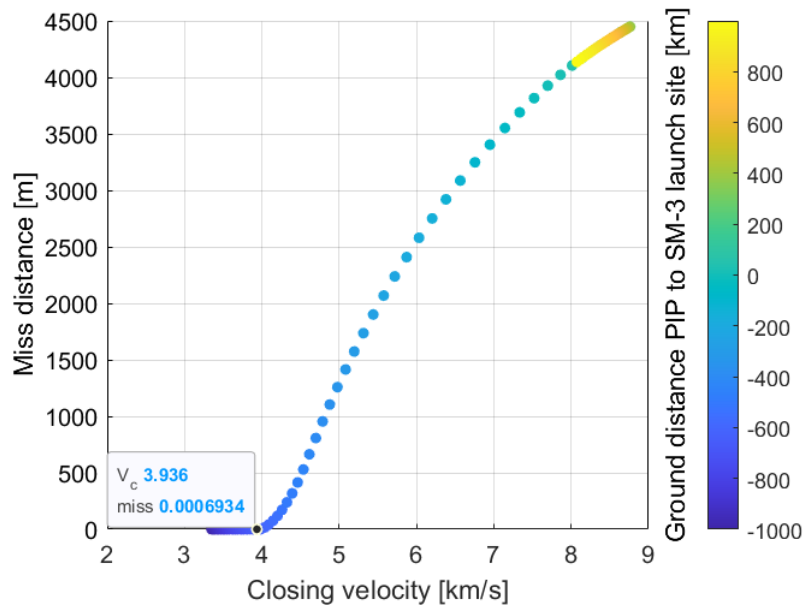

Figure 4.8: Miss distance as a function of V_c.

4.3.2 Target Range

Figure 4.9 and 4.10 show the results from the final 2D simulation. Figure 4.9 shows that the maximum target range that the Block IIA can handle is 6,817 km for a relative flight path angle of $28° < \gamma_{TM} < 38°$ (chosen to be similar to the result in Figure 4.7). The closing velocity at this point is 3.91 $\frac{km}{s}$. This is largely in line with the findings in the previous section, in which a similar intercept geometry yielded a maximum $V_c = 3.94 \frac{km}{s}$ for a target hit. Moreover, the maximum ICBM range found for an intercept is greater than the one adopted in the previous section. This difference is due to fluctuations in γ_{TM} for different SM-3 launch sites.
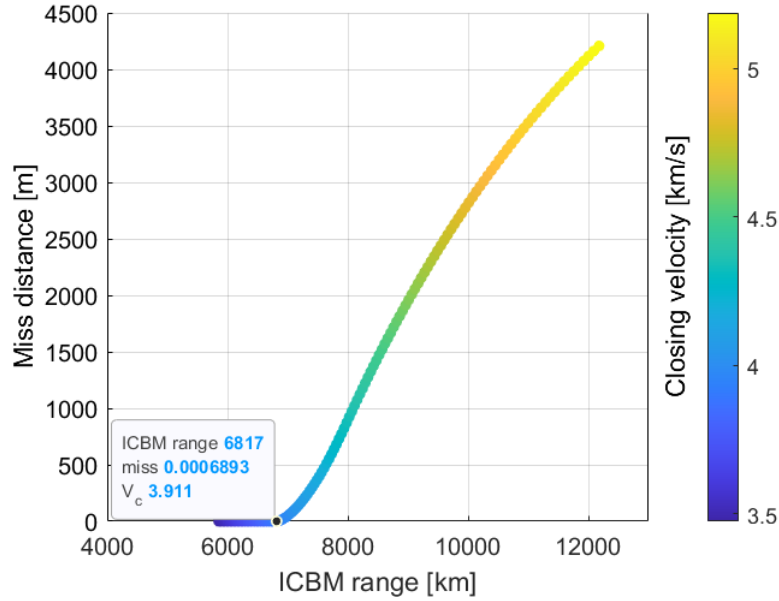

Figure 4.9: Miss distance as a function of target range $(28° < \gamma_{TM} < 38°)$.

Figure 4.10 shows the separate impact of increased target offset and V_c on the miss distance for an ICBM intercept. The difference in slope between the yellow and red curve indicate that the higher V_c as a result of greater target range impacts the miss distance slightly less than the increased target offset. However, neither increased target offset or closing velocity for intercepting ICBMs can be neglected. The figure also illustrates that the sum of the red and yellow curve is significantly less than the total miss distance. From this, one can conclude that the effects of both V_c and target offset strengthen each other.
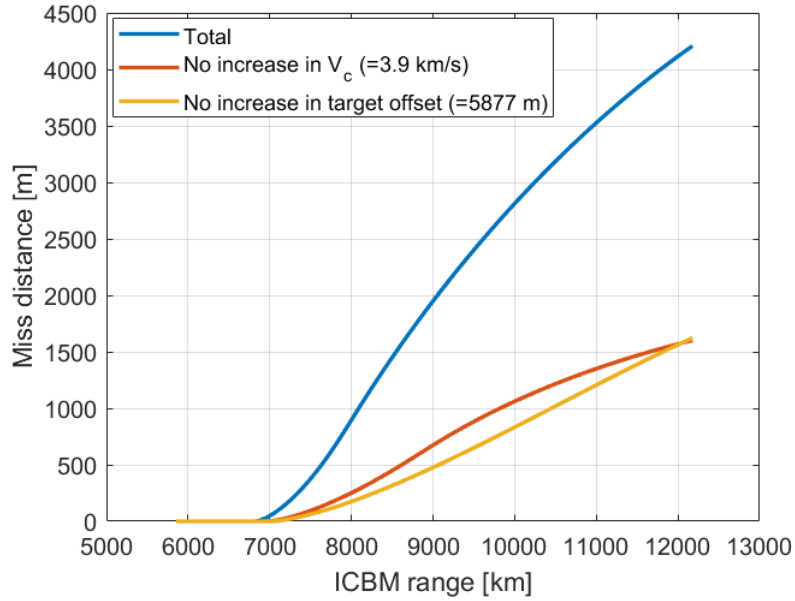
Figure 4.10: Miss distance for no increase in target offset and no increase in V_c ($28° < \gamma_{TM} < 38°$).

4.4 Block IIA ICBM Interceptions 3D

4.4.1 FTM-44

Figure 4.11 depicts the estimated FTM-44 terminal phase intercept geometry in the ENU local coordinate system. From this figure it becomes clear that the interceptor approached its target from the side. Hereby, creating a situation far from the $\gamma_{TM} = 180°$ head-on engagement which yielded the most pressing situation in the 2D simulations. Additionally, the target to missile range and the closing velocity that corresponds to the intercept geometry are depicted in Figure 4.12 (a) and (b), respectively.
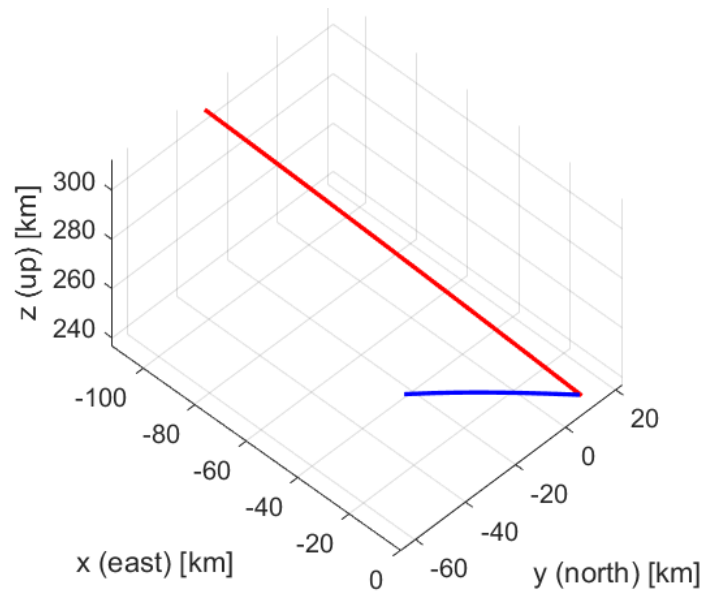

Figure 4.11: FTM-44 terminal phase intercept geometry.

(a) R_{TM}.   (b) V_c.
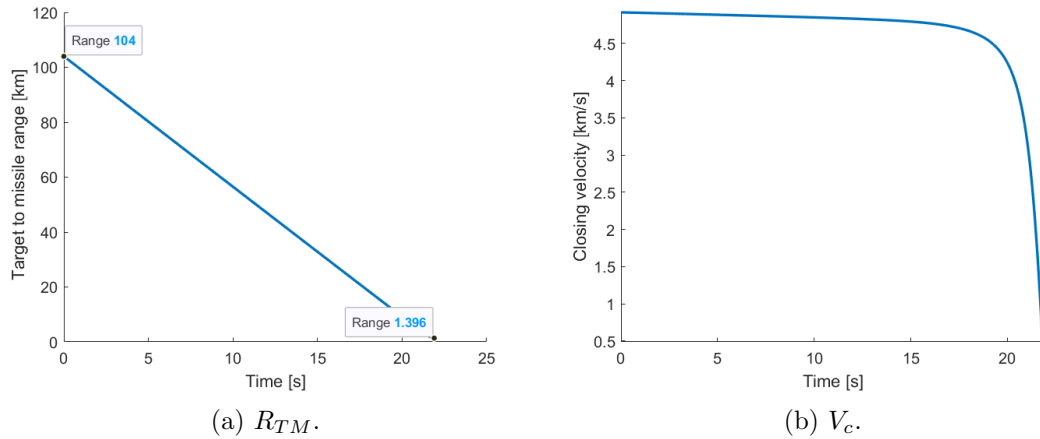
Figure 4.12: FTM-44 closing velocity and target to missile range.

Figure 12 (a) clearly indicates the R_{IR} adopted for this simulation, 104 km. The miss distance in the simulation is 1.4 km, as indicated by the data tip. Figure 12 (b) shows that the closing velocity during the terminal phase guidance is about 4.8 $\frac{\text{km}}{\text{s}}$.

(a) ΔV.   (b) n_a.
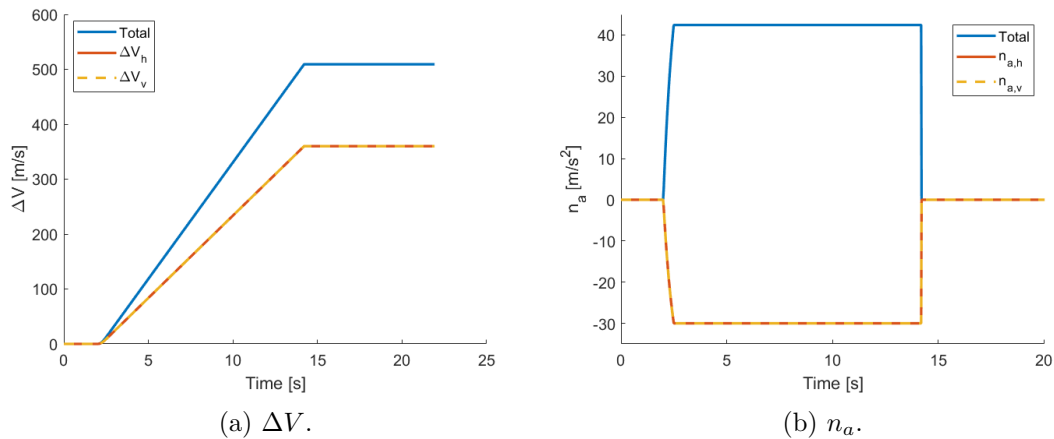
Figure 4.13: FTM-44 divert parameters.

Furthermore, Figure 4.13 shows the divert and lateral acceleration adopted throughout the terminal phase. Due to the equal offset in the directions perpendicular to λ_v and λ_h, the lateral accelerations and total diverts in these directions are equal as well. From Figure 4.13 (b) it can be derived that the maximum lateral acceleration is applied right after t_{ID}. The KV holds this acceleration until the maximum total divert is reached. After this, the acceleration in both $\vec{n}_h$ and $\vec{n}_v$ directions becomes zero.

Laslty, Figure 4.12 shows that the FTM-44 BMD test would be unsuccessful for the KV IR range, divert capacity and target offset adopted throughout this research. This yields the question as to what caused the FTM-44 to be successful nonetheless. The next sections will elaborate on the possible factors that could have led to an intercept after all, starting with a different SM-3 launch site.

4.4.2 SM-3 Launch Site in the FTM-44 BMD Test

Figure 4.14 shows a map of possible SM-3 launch sites in degrees longitude and latitude relative to the PIP. In this map, an SM-3 launch site in the yellow area yields a miss and an SM-3 launch site in the blue area results in a hit. The green arrow indicates the SM-3 launch site adopted during the FTM-44 BMD test that follows from Section 2.3. It is very unlikely for the SM-3 launch site to have been in the area indicated blue as this would have been outside the navigational warning area depicted in Figure 2.7. Therefore, there should have been other factors in play to cause the hit that was accomplished during the FTM-44 flight event.
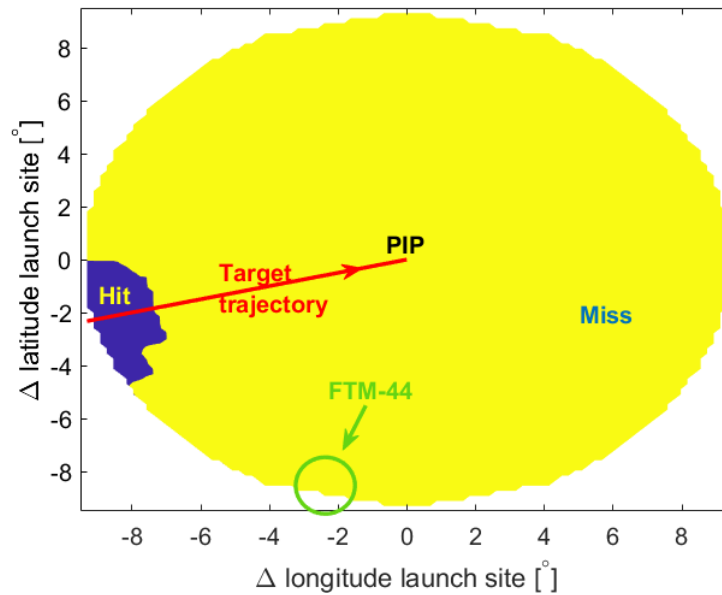

Figure 4.14: Hit or miss in FTM-44 test as a function of SM-3 launch site relative to PIP.

4.4.3 IR Range, Target Offset and PIP in the FTM-44 BMD Test

Assuming that the divert capacity and IR seeker's NEFD found for the Block IIA KV are reliable, the FTM-44 was most likely a success due to smaller target offset, greater target signature (and therefore IR range), another PIP altitude, or a combination of these factors.

Figure 4.15 shows the influence of the target offset and IR range on the final result of the engagement. Similar to Figure 4.14, in this plot the blue combinations of R_{IR} - $o_{\perp \lambda_p}$ yield an intercept and the yellow combinations result in a miss. The figure clearly shows that, given a greater target signature (RV temperature and size) and/or smaller target offset, the FTM-44 BM engagement would be a success. Although this situation might be possible in some actual ICBM engagements, chances are relatively small. Furthermore, an ICBM target signature, target offset combination cannot be expected to be as favourable as the blue shaded area in Figure 4.15. After all, when engaging an ICBM target it is vital for the defending party to be sure about the outcome of the event.
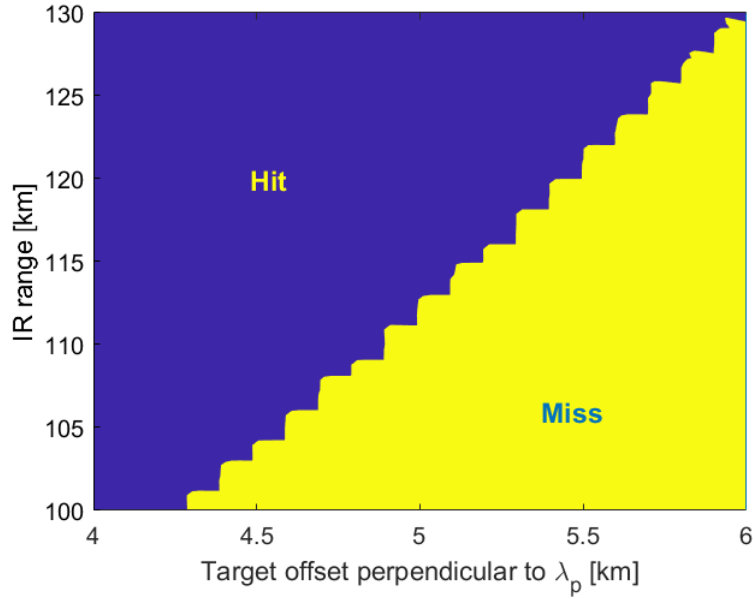
Figure 4.15: Hit or miss in FTM-44 test as a function of IR range and target offset.

Lastly, Figure 4.16 shows the influence of the chosen PIP on the final result of the FTM-44 engagement. This figure shows that the KV's chances increase slightly for a lower PIP altitude. This is due to the fact that, for a smaller PIP altitude, the KV approaches its target even more in the form of a tail-chase engagement, decreasing the closing velocity during the terminal phase. Still, the choice of PIP does not affect the outcome of the BMD test as much as the target offset. Even for a minimum PIP altitude, the adopted IR range would still yield a failed attempt to intercept the ICBM dummy. Therefore, this could not have been the determining factor for causing an intercept in the FTM-44 flight event.
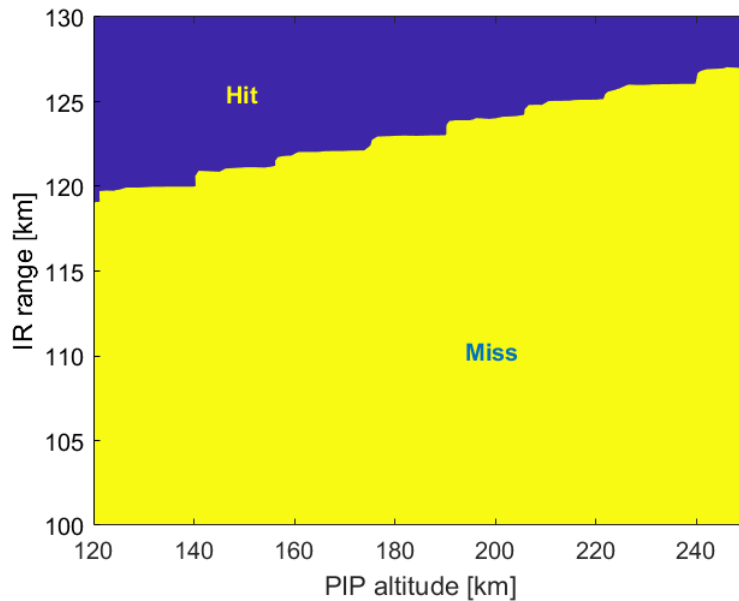

Figure 4.16: Hit or miss in FTM-44 test as a function of IR range and PIP altitude.

5. Conclusion and Recommendations

The purpose of this research was to investigate the strategic meaning of the FTM-44 flight event concerning U.S. BMD. To do so, a literature review was conducted on feasible SM-3 specifications. In addition, several simulations of BMD engagements were done to build on the literature review.

From the literature review, several conclusion can be drawn. Most remarkable is the SM-3 Block IIA burnout velocity of 3.3 - 3.8 $\frac{km}{s}$ derived from the FTM-44 planning parameters as this is a significantly lower value than the 4.5 $\frac{km}{s}$ stated by current literature. Also, using the same planning parameters it was concluded that the intercept geometry of the FTM-44 event was indeed chosen in a way in which the interceptor approached its target from the side and not head-on.

Secondly, a couple of general relations between intercept parameters were derived. It was found that target offset only matters when it is perpendicular to the predicted LOS. Furthermore, a doubling in this target offset perpendicular to LOS yields a doubling in the lateral acceleration and total divert applied by the KV for a target kill. Also, the SM-3 launch site is crucial when it comes to the KV's chance of success, as it defines the closing velocity in the terminal phase. This is, next to target offset and IR seeker range, one of the main factors to determine the divert capacity needed for an intercept.

Next, some additional KV specifications were derived by means of simulating standard engagements that should result in successful interceptions based on the KV's capabilities claimed by the manufacturer. These include the Block IIA's IR seeker sensitivity and divert capabilities. Evidently, the adopted KV specifications and intercept parameters could not have led to a successful intercept in the FTM-44 scenario, even though the intercept geometry chosen was rather expedient. Therefore, the actual FTM-44 scenario was either a lucky shot or manipulated in a way that is favourable for an intercept. This could have been accomplished by adopting a larger target RV than can be expected from a realistic ICBM target. Another option for increasing the IR seeker's range is increasing the target's temperature. Lastly, the target offset could have been decreased by choosing and placing external sensors in a way that yields optimal observations.

Whether one of these actions was taken or not, the events on November 16, 2020 cannot be generalised as to the SM-3 Block IIA would be capable of protecting U.S. soil from ICBM threats. This is because the relatively simple ICBM target (in one way or the other) adopted during the FTM-44 test, accompanied by a rather favourable geometry. When dealing with actual threats, this geometry cannot be expected to always be as convenient. Also, actual ICBM threats (for instance from North-Korea or Russia aiming for the U.S. West Coast) include greater target velocities than the dummy ICBM's RV in the FTM-44 engagement. The flight event was a show of force that cannot be backed up when it comes down to it. To answer the research question, the FTM-44 does not represent strategic significance concerning the problem of U.S. BMD.

The current research has presented some insight into the capabilities of the SM-3 against various threat ranges. However, many parameters had to be estimated based on limited public sources, as no official specifications of the SM-3 were available. This yields some limitations, including the divert capability accepted. This was most likely an upper estimate.

Future research could include an iteration process in which more feasible combinations between IR seeker range and divert capabilities are investigated. Such an iteration process could eventually bring the SM-3 IR seeker's and DACS' specifications closer to the actual SM-3's capabilities. Nevertheless, this paper forms a good framework for conducting such an additional study.

Furthermore, target offset should be investigated more thoroughly, as the target offset adopted throughout this paper includes one major assumption in particular. That is, a constant target offset due to limitations in radar accuracy. It is very well possible that the target offset adopted is either a lower or an upper estimate in some particular scenarios. Be that as it may, the offset expression stated still yields realistic values that should be considered while performing BMD.

Lastly, the IR seeker's resolution and target filtering have not been discussed in this research. Including these topics in future research might reveal insights into the different ways in which target types influence the IR seeker's range. Besides, it could increase understanding about the behaviour of the time parameter indicated as t_{ID} throughout the current research.

References

[1] A. Augustyn, "Encyclopedia Britannica," 2020. [Online] Available at: https://www.britannica.com/technology/ballistic-missile. [Accessed Dec. 10, 2020].

[2] S. Gearhart, "Testing the SM-3 Kinetic Warhead in the Guidance System Evaluation Laboratory," John Hopkins APL Technical Digest, vol. 22, no. 3, p. 302-310, 2001.

[3] R. Savelsberg and M. Voskuijl, "BSc final project proposal: Divert capacity and lateral acceleration required for exo-atmospheric ballistic missile intercepts," 2020.

[4] M. Eckstein, "MDA to Use Destroyer USS John Finn for Defense-of-Hawaii Missile Intercept Test," USNI News, 2020. [Online], Available at: https://news.usni.org/2020/08/05/mda-to-use-destroyer-uss-john-finn-for-defense-of-hawaii-missile-intercept-test. [Accessed Feb. 5, 2021].

[5] United States Navy, "U.S. Successfully Conducts SM-3 Block IIA Intercept Test Against Intercontinental Ballistic Missile," Nov. 17, 2020. [Online]. Available at: https://www.navy.mil/Press-Office/Press-Releases/display-pressreleases/Article/2417589/us-successfully-conducts-sm-3-block-iia-intercept-test-against-intercontinental/. [Accessed Dec. 10, 2020].

[6] United States Missile Defense Agency, "FTM-44 Mission Video," Nov. 17, 2020. [Online]. Available: https://www.dvidshub.net/unit/MDA. [Accessed Dec. 10, 2020].

[7] J. Bos. "An investigation of the divert-capacity of the KV of an anti-ballistic missile," MSc. thesis, Cranfield Defence and Security, Shrivenham, U.K. 2019

[8] P. Zarchan, "Tactical And Strategic Missile Guidance," 6th ed. Reston, VA: American Institute of Aeronautics and Astronautics, 2012.

[9] K. W. Naumann et al.,"Green Gelled Propellant Gas Generator for High-Performance Divert- and Attitude Control Systems," 2016.

[10] J. Seitzman, "Rocket Propulsion Basics Thrust and Impulse," 2018.

[11] S. Robinson, "Navy Theater-Wide Defense AEGIS LEAP Intercept (ALI)/STANDARD Missile Three (SM-3) Flight Test Program Overview," In Proc. AIAA/BMDO Technology Readiness Conference and Exhibit, 1997.

[12] D. Frem, "A Reliable Method for Predicting the Specific Impulse of Chemical Propellants," J. Aerosp Technol Manag, 2018. 10:e3318. doi: 10.5028/jatm.v10.945.

[13] G. Lengellé, J. Duterque and J. Trubert, "Combustion of Solid Propellants," Office national d'études et de recherches aérospatiales (ONERA), 2002.

[14] G. Sullins, "Exo-atmospheric Intercepts: Bringing New Challenges to Standard Missile," John Hopkins APL Technical Digest, vol. 22, no. 3, p. 260-274, 2001.

[15] E. Evans, "Missile Defense Technology," MIT Lincoln Laboratory, Lexington, MA, 1999.

[16] C. Payne, "Principles of naval weapon systems," Annapolis, Md.: Naval Institute Press, 2010.

[17] A. Sessler, "Countermeasures," Union of Concerned Scientists/MIT, 2000.

[18] R. Pilgrim, "LWIR Sensors in Ballistic Missile Defense Systems (BMDS)," Huntsville, Alabama, 2005.

[19] G. Lewis, "Strategic Capabilities of SM-3 Block IIA Interceptors," June 30, 2016, Mostly Missile Defense, 2016.

[20] J. Lewis, "Video Analysis of the Reentry of North Korea's July 28, 2017 Missile Test," Arms Control Wonk, 2018.

[21] A. Javid, "Iran Emad guided & controlled ballistic missile, 4 Cam onboard," Oct. 11, 2015. [Online Video] Available at: https://www.youtube.com/watch?v=ci1H4zw_6VA. [Accessed March 9, 2020].

[22] J. Pike, "Boost Phase," Globalsecurity.org, 2011. [Online]. Available at: https://www.globalsecurity.org/space/systems/boost-phase.htm. [Accessed March 14, 2021].

[23] D. Nguyen, B. Cho, C. Seo, J. Park and D. Lee, "Analysis of the Optimal Frequency Band for a Ballistic Missile Defense Radar System," Journal of Electromagnetic Engineering and Science, vol. 18, no. 4, p. 231-241, 2018.

[24] M. Langbroek, "SM-3 Block IIA Missile Defense test FTM-44 against an ICBM-class target imminent, 17-19 November 2020 [UPDATED]," Sattrackcam, Nov. 15, 2020. [Online]. Available at: https://sattrackcam.blogspot.com/2020/11/sm-3-block-iia-missile-defense-test-ftm.html. [Accessed Feb. 4, 2021].

[25] R. Savelsberg, "Program for plotting 2D ballistic missile trajectories using closed-form solutions to the BM equations of motion in polar coordinates," Netherlands Defence Academy, 2019.

Appendices

A. Analytical Derivations

A.1 IR Incidence E

In this section of the appendix the target's IR flux at the seeker is derived, starting with the IR radiation transfer function for a Lambertian source:

$$I_{e,\Omega,\lambda} = \frac{\epsilon A_{proj}}{\pi} M_{e,\lambda} \tag{A.1}$$

with $I_{e,\Omega,\lambda}$ the spectral radiant intensity in $[\frac{\text{W}}{\text{sr}\cdot\text{m}}]$. A_{proj} the projected target area in the direction of the seeker in $[\text{m}]$ and ϵ the target's emissivity compared to a black body equivalent. Lastly, $M_{e,\lambda}$ is the spectral exitance of the source in $[\frac{\text{W}}{\text{m}^3}]$. According to the Stefan-Boltzmann Law:

$$M = \int_0^\infty M_{e,\lambda}\mathrm{d}\lambda = \sigma T^4 \tag{A.2}$$

with M the radiant exitance in $[\frac{\text{W}}{\text{m}^2}]$, σ the Stefan-Boltzmann constant of $5.67 \cdot 10^{-8}\ \frac{\text{W}}{\text{m}^2\text{K}^4}$ and T the source's temperature in $[\text{K}]$. In accordance with Equation A.2, integrating Equation A.1 yields:

$$I_{e,\Omega} = \frac{\epsilon A_{proj}}{\pi} \sigma T^4 \tag{A.3}$$

with $I_{e,\Omega}$ the radiant intensity in $[\frac{\text{W}}{\text{sr}}]$.

$$\Phi_e = \frac{\epsilon A_{proj}}{\pi} \sigma T^4 \Omega \tag{A.4}$$

In Equation A.4, Φ_e is the radiant flux at the seeker's aperture in $[\text{W}]$. Furthermore, the solid angle occupied by the detector Ω in $[\text{sr}]$ is:

$$\Omega = \frac{A_{det}}{R^2} \tag{A.5}$$

with A_{det} the detector's aperture area in $[\text{m}^2]$ and R the distance between target and the seeker in $[\text{m}]$. Substituting Equation A.5 into Equation A.4 yields:

$$\Phi_e = \frac{\epsilon A_{proj}}{\pi} \sigma T^4 \frac{A_{det}}{R^2} \tag{A.6}$$

$$E = \frac{\epsilon A_{proj} \sigma T^4}{\pi R^2} \tag{A.7}$$

with incidence E the flux density at the seeker's aperture in $[\frac{\text{W}}{\text{m}^2}]$. However, since an IR seeker can only detect within a certain bandwidth, the integration interval used in Equation A.2 is not $[0, \infty]$, but smaller. To take this into account, a correction factor F was added to Equation A.7.

$$E = \frac{\epsilon A_{proj} \sigma T^4 F}{\pi R^2} \tag{A.8}$$

A.2 Closing Velocity V_c

In this section of the appendix the closing velocity between missile and target is derived.

$$V_c = -\frac{\mathrm{d}}{\mathrm{d}t} R_{TM} \tag{A.9}$$

Substituting for $R_{TM} = \sqrt{R_{TM_x}^2 + R_{TM_y}^2 + R_{TM_z}^2}$ yields:

$$V_c = -\frac{\mathrm{d}}{\mathrm{d}t} \sqrt{R_{TM_x}^2 + R_{TM_y}^2 + R_{TM_z}^2} \tag{A.10}$$

$$V_c = -\frac{1}{2\sqrt{R_{TM_x}^2 + R_{TM_y}^2 + R_{TM_z}^2}} \left(2R_{TM_x}\frac{\mathrm{d}}{\mathrm{d}t}(R_{TM_x}) + 2R_{TM_y}\frac{\mathrm{d}}{\mathrm{d}t}(R_{TM_y}) + 2R_{TM_z}\frac{\mathrm{d}}{\mathrm{d}t}(R_{TM_z}) \right) \tag{A.11}$$

$$V_c = -\frac{R_{TM_x}V_{TM_x} + R_{TM_y}V_{TM_y} + R_{TM_z}V_{TM_z}}{R_{TM}} \tag{A.12}$$

A.3 Angular Velocity of Horizontal LOS $\dot{\lambda}_h$

In this section of the appendix the angular velocity of the horizontal LOS $\dot{\lambda}_h$ is derived.

$$\lambda_h = \arctan\left(\frac{R_{TM_y}}{R_{TM_x}}\right) \tag{A.13}$$

$$\frac{\mathrm{d}}{\mathrm{d}t}(\arctan(f(t))) = \frac{1}{1 + f(t)^2}\frac{\mathrm{d}}{\mathrm{d}t}f(t) \tag{A.14}$$

$$\dot{\lambda}_h = \frac{\mathrm{d}}{\mathrm{d}t}\left(\arctan\left(\frac{R_{TM_y}}{R_{TM_x}}\right)\right) = \frac{1}{1 + \left(\frac{R_{TM_y}}{R_{TM_x}}\right)^2}\frac{\mathrm{d}}{\mathrm{d}t}\left(\frac{R_{TM_y}}{R_{TM_x}}\right) \tag{A.15}$$

$$\frac{\mathrm{d}}{\mathrm{d}t}\left(\frac{R_{TM_y}}{R_{TM_x}}\right) = \frac{R_{TM_x}V_{TM_y} - R_{TM_y}V_{TM_x}}{R_{TM_x}^2} \tag{A.16}$$

$$\dot{\lambda}_h = \frac{1}{1 + \left(\frac{R_{TM_y}}{R_{TM_x}}\right)^2}\frac{R_{TM_x}V_{TM_y} - R_{TM_y}V_{TM_x}}{R_{TM_x}^2} \tag{A.17}$$

$$\dot{\lambda}_h = \frac{R_{TM_x}^2}{R_{TM_x}^2 + R_{TM_y}^2}\frac{R_{TM_x}V_{TM_y} - R_{TM_y}V_{TM_x}}{R_{TM_x}^2} \tag{A.18}$$

$$\dot{\lambda}_h = \frac{R_{TM_x}V_{TM_y} - R_{TM_y}V_{TM_x}}{R_{TM_x}^2 + R_{TM_y}^2} \tag{A.19}$$

A.4 Angular Velocity of Vertical LOS $\dot{\lambda}_v$

In this section of the appendix the angular velocity of the vertical LOS $\dot{\lambda}_v$ is derived.

$$\lambda_v = \arctan\left(\frac{R_{TM_z}}{\sqrt{R_{TM_x}^2 + R_{TM_y}^2}}\right) \tag{A.20}$$

$$\frac{\mathrm{d}}{\mathrm{d}t}(\arctan(f(t))) = \frac{1}{1 + f(t)^2}\frac{\mathrm{d}}{\mathrm{d}t}f(t) \tag{A.21}$$

$$\dot{\lambda}_v = \frac{1}{1 + \left(\dfrac{R_{TM_z}}{\sqrt{R_{TM_x}^2 + R_{TM_y}^2}}\right)^2}\frac{\mathrm{d}}{\mathrm{d}t}\frac{R_{TM_z}}{\sqrt{R_{TM_x}^2 + R_{TM_y}^2}} \tag{A.22}$$

$$\frac{\mathrm{d}}{\mathrm{d}t}\frac{R_{TM_z}}{\sqrt{R_{TM_x}^2 + R_{TM_y}^2}} = \frac{\sqrt{R_{TM_x}^2 + R_{TM_y}^2}\frac{\mathrm{d}}{\mathrm{d}t}R_{TM_z} - R_{TM_z}\frac{\mathrm{d}}{\mathrm{d}t}\sqrt{R_{TM_x}^2 + R_{TM_y}^2}}{R_{TM_x}^2 + R_{TM_y}^2} \tag{A.23}$$

$$\frac{\mathrm{d}}{\mathrm{d}t}\frac{R_{TM_z}}{\sqrt{R_{TM_x}^2 + R_{TM_y}^2}} = \frac{\sqrt{R_{TM_x}^2 + R_{TM_y}^2}V_{TM_z} - R_{TM_z}\dfrac{R_{TM_x}V_{TM_x} + R_{TM_y}V_{TM_y}}{\sqrt{R_{TM_x}^2 + R_{TM_y}^2}}}{R_{TM_x}^2 + R_{TM_y}^2} \tag{A.24}$$

$$\frac{\mathrm{d}}{\mathrm{d}t}\frac{R_{TM_z}}{\sqrt{R_{TM_x}^2 + R_{TM_y}^2}} = \frac{(R_{TM_x}^2 + R_{TM_y}^2)V_{TM_z} - R_{TM_z}(R_{TM_x}V_{TM_x} + R_{TM_y}V_{TM_y})}{R_{TM_x}^2 + R_{TM_y}^2} \tag{A.25}$$

$$\dot{\lambda}_v = \frac{1}{1 + \left(\dfrac{R_{TM_z}}{\sqrt{R_{TM_x}^2 + R_{TM_y}^2}}\right)^2}\frac{(R_{TM_x}^2 + R_{TM_y}^2)V_{TM_z} - R_{TM_z}(R_{TM_x}V_{TM_x} + R_{TM_y}V_{TM_y})}{R_{TM_x}^2 + R_{TM_y}^2} \tag{A.26}$$

$$\dot{\lambda}_v = \frac{(R_{TM_x}^2 + R_{TM_y}^2)V_{TM_z} - R_{TM_z}(R_{TM_x}V_{TM_x} + R_{TM_y}V_{TM_y})}{(R_{TM_x}^2 + R_{TM_y}^2 + R_{TM_z}^2)\sqrt{R_{TM_x}^2 + R_{TM_y}^2}} \tag{A.27}$$
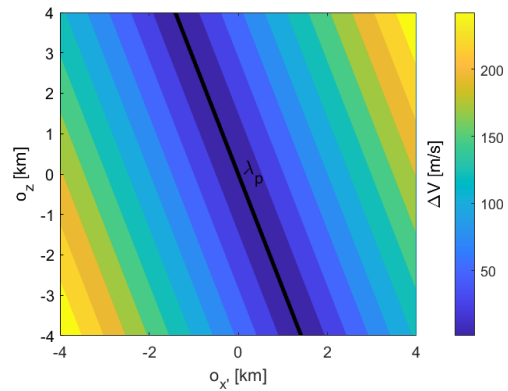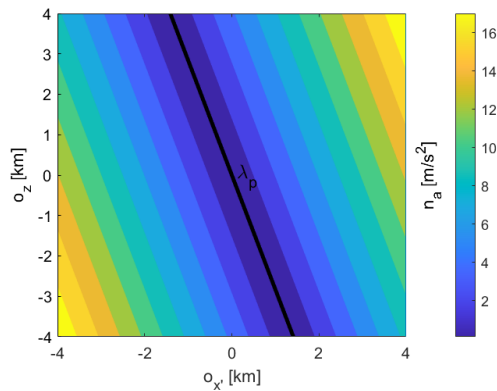
B. Raw Data

B.1 Target Offset

In this section of the appendix the raw results for the divert capacity as a function of target offset for various intercept geometries are included.
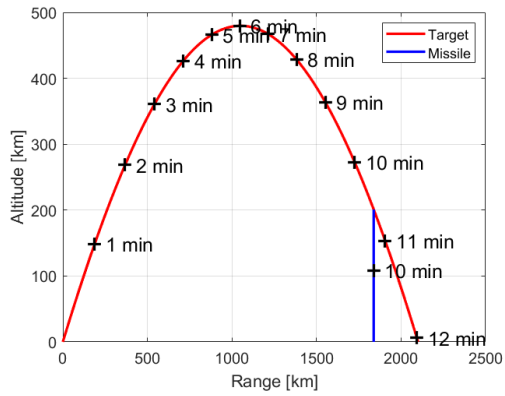

(a) Ballistic trajectories.

(b) ΔV.
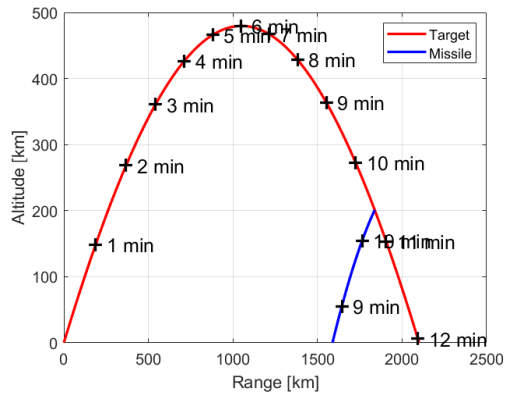
(c) Maximum n_a.

Figure B.1: ΔV and maximum n_a as a function of target offset for a ground distance PIP to launch site SM-3 of -250 km.
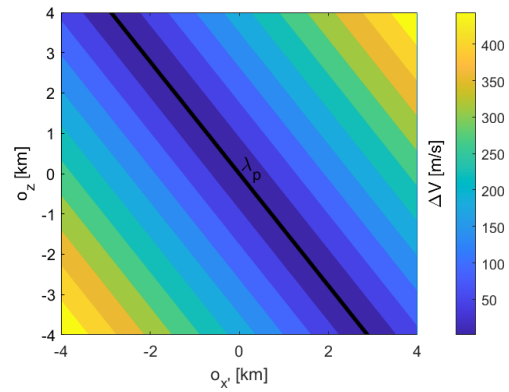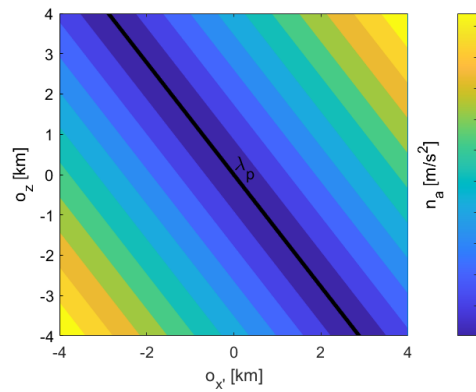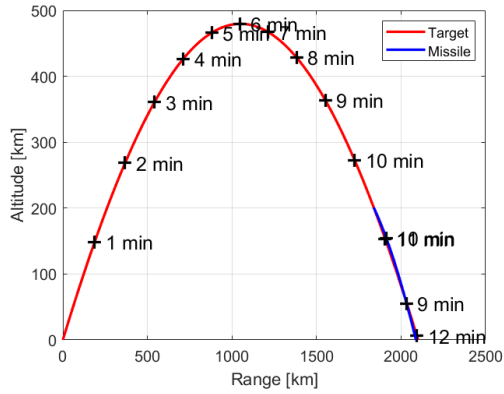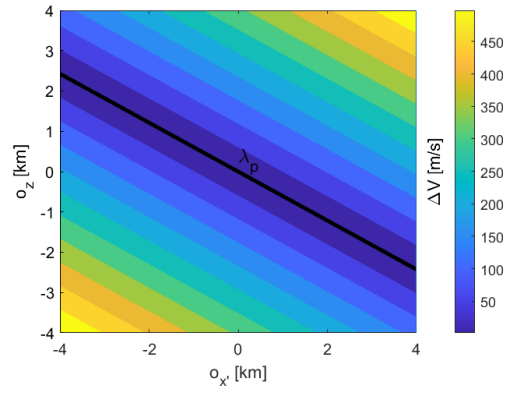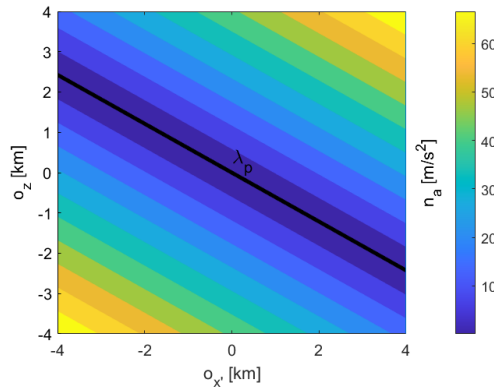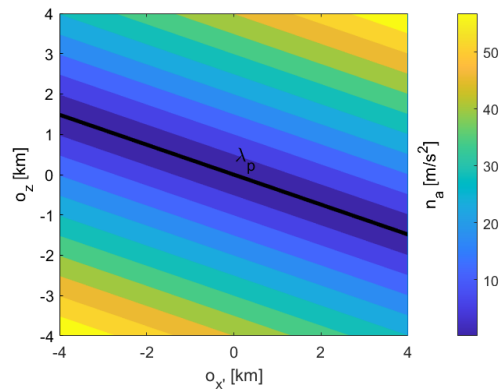
(a) Ballistic trajectories.

(b) ΔV.

(c) Maximum n_a.

Figure B.2: ΔV and maximum n_a as a function of target offset for a ground distance PIP to launch site SM-3 of 0 km.

(a) Ballistic trajectories.

(b) ΔV.

(c) Maximum n_a.

Figure B.3: ΔV and maximum n_a as a function of target offset for a ground distance PIP to launch site SM-3 of 250 km.

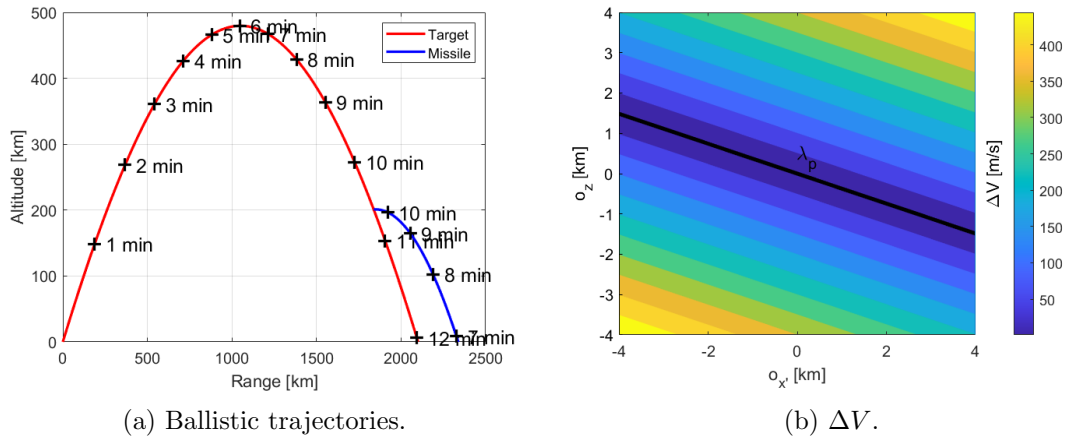(a) Ballistic trajectories.

(b) ΔV.

(c) Maximum n_a.

Figure B.4: ΔV and maximum n_a as a function of target offset for a ground distance PIP to launch site SM-3 of 500 km.

C. Files

In this appendix firstly, the Matlab® code used for the research will be listed. Listings C.1 and C.4 form the body of the the 2D model and the 3D model, respectively. The other files listed (reversed dynamics from PIP and the actual terminal phase guidance) are called upon at a certain point in these codes. In addition, the Simulink® block diagrams that represent the terminal phase missile guidance are included in Appendices C.3 and C.4.

C.1 Matlab® Code Listings for the 2D Model

Listing C.1: m-file 'SM3_vs_BM_trajectories2D.m'.

```matlab
1  %Code for simulating terminal phase SM-3 KV engagement in 2D
2  %Noah Stam
3  %Netherlands Defence Academy
4  %February 2021
5
6  if Distance_target_SM3≠prev_Distance_target_SM3 || Distance_target ≠...
       prev_Distance_target || Vburn_BM≠prev_Vburn_BM
7      %Only calculate trajectories if launchsite or Vbo has changed
8      intercept_ballistic_trajectory2D
9
10     %Endstates
11     %Missile
12     x0m_PIP=1e-9;    %+1e-9 to prevent division by RTM=0
13     z0m_PIP=h_SM3(end);
14     Vx0m_PIP=velocity_SM3(end)*cos(pitch_SM3(end));
15     Vz0m_PIP=velocity_SM3(end)*sin(pitch_SM3(end));
16     %Target
17     x0t_PIP=0;
18     z0t_PIP=h_BM(Npip);
19     Vx0t_PIP=velocity_BM(Npip)*cos(pitch_BM(Npip));
20     Vz0t_PIP=velocity_BM(Npip)*sin(pitch_BM(Npip));
21  end
22
23  driverfile_reversed_dynamics2D
24
25  %Set previous values for launchsite SM3 and IR Vburn for next iteration
26  prev_Distance_target_SM3=Distance_target_SM3;
27  prev_Distance_target=Distance_target;
28  prev_Vburn_BM=Vburn_BM;
29
30  %Use calculated begin conditions to start Simulink Model
31  driverfile2D
```

Listing C.2: m-file 'driverfile_reversed_dynamics2D.m'.

```matlab
1  %Code to determine the initial conditions of the terminal phase in 2D
2
3  %Initial conditions
4  x0m=x0m_PIP;
5  z0m=z0m_PIP;
6  Vx0m=-Vx0m_PIP;
7  Vz0m=-Vz0m_PIP;
8  x0t=x0t_PIP;
9  z0t=z0t_PIP;
10 Vx0t=-Vx0t_PIP;
11 Vz0t=-Vz0t_PIP;
12
13 %Gravity
14 R_earth=6371222;        %Earth's Radius [m]
15 GM=398600.4418e9;       %Standard gravitational parameter [m^3/s^2]
16
17 %Guidance parameters
18 N=0;                    %Nav. ratio for no guidance
19 Tc=10;                  %Variables that don't matter without guidance
20
21 %Simulation
22 te=4000;                %Max. length simulation [s]
23 dtmax=0.001;            %Max. length timestep [s]
24 T0=0;                   %Start of simulation [s]
25
26 %Determine LOS angle for offset
27 RTM_guidance=1e3;
28 sim('terminalphaseguidancemodel2d')
29 lambda=LOS(end);
30 if offsetconstant==0
31     offsetLOS=sqrt(25*(t_BM(Npip)-(t_BM(end)-t_BM(1))*0.1667)^2+914^2);
32 end
33 xo=-offsetLOS*sin(lambda);
34 zo=offsetLOS*cos(lambda);
35
36 %Actual reversed dynamics including target offset
37 %General expression for target offset as a function of BM RV flight time
38 x0t=x0t-xo;
39 z0t=z0t-zo;
40 RTM_guidance=RIR;
41 sim('terminalphaseguidancemodel2d')
42
43 %Find start conditions for guidance model
44 x0t=xt(end-1);
45 z0t=zt(end-1);
46 Vx0t=-vxt(end-1);
47 Vz0t=-vzt(end-1);
48 x0m=xm(end-1);
49 z0m=zm(end-1);
50 Vx0m=-vxm(end-1);
51 Vz0m=-vzm(end-1);
```

Listing C.3: m-file 'driverfile2D.m'.

```matlab
1  %Driverfile missile guidance in 2D
2
3  %Guidance parameters
4  Tc=0.5;                    %Timeconstant autopilot interceptor [s]
5  N=3;                       %Eff. nav. ratio for ballistic trajectories [-]
6
7  %Simulation
8  te=4000;                   %Max. length simulation [s]
9  dtmax=0.001;               %Max. length timestep [s]
10 T0=0;                      %Start of simulation [s]
11 sim('terminalphaseguidancemodel2d');
12
13 %Postprocessing
14 miss=min(RTM);
15 %Determine gammaTM
16 pitchm=atan2(vzm,vxm);
17 pitcht=atan2(vzt,vxt);
18 if pitchm(1) >= -0.5*pi && pitchm(1) <= pi
19     gammaTM=abs(pitcht-pitchm)*180/pi;
20 else
21     gammaTM=abs(pitcht-2*pi-pitchm)*180/pi;
22 end
```

C.2 Matlab® Code Listings for the 3D Model

Listing C.4: m-file 'SM3_vs_BM_trajectories3D.m'.

```
1  %Code for simulating terminal phase SM-3 KV engagement in 3D
2  %Noah Stam
3  %Netherlands Defence Academy
4  %March 2021
5
6  %Uses 'intercept_ballistic_trajectory.m' for calculating BM and ...
       interceptor
7  %trajectories
8  %Ralph Savelsberg
9  %Netherlands Defence Academy,
10 %February 2021
11
12 intercept_ballistic_trajectory
13
14 %Endstate of missile and target x=east y=north z=up
15 %Interceptor
16 x0m_PIP=1e-9;          %+1e-9 is to prevent division by zero (RTM=0)
17 y0m_PIP=1e-9;
18 z0m_PIP=h_s(end);
19 Vx0m_PIP=V_east_s(end);
20 Vy0m_PIP=V_north_s(end);
21 Vz0m_PIP=V_up_s(end);
22 %Target
23 x0t_PIP=0;
24 y0t_PIP=0;
25 z0t_PIP=h_tgt(Npip);
26 Vx0t_PIP=V_east(Npip);
27 Vy0t_PIP=V_north(Npip);
28 Vz0t_PIP=V_up(Npip);
29
30 %Calculate reversed dynamics from PIP in flat Earth coordinate system
31 driverfile_reversed_dynamics3D
32 %Use calculated begin conditions to start Simulink Model
33 driverfile3D
```

Listing C.5: m-file 'driverfile_reversed_dynamics3D.m'.

```matlab
 1  %Code to determine the initial conditions of the terminal phase in 3D
 2  x0m=x0m_PIP;
 3  y0m=y0m_PIP;
 4  z0m=z0m_PIP;
 5  Vx0m=-Vx0m_PIP;
 6  Vy0m=-Vy0m_PIP;
 7  Vz0m=-Vz0m_PIP;
 8  x0t=x0t_PIP;
 9  y0t=y0t_PIP;
10  z0t=z0t_PIP;
11  Vx0t=-Vx0t_PIP;
12  Vy0t=-Vy0t_PIP;
13  Vz0t=-Vz0t_PIP;
14
15  %Parameters
16  R_earth=6371222;          %Earth's Radius [m]
17  GM=398600.4418e9;         %Standard gravitational parameter [m^3/s^2]
18  N=0;                      %Nav. ratio for no guidance
19  Tc=12345;                 %Variables that don't matter without guidance
20  te=4000;                  %Max. length simulation [s]
21  dtmax=0.001;              %Max. length timestep [s]
22  T0=0;                     %Start of simulation [s]
23
24  %Determine LOS angle for offset
25  RTM_guidance=1e3;
26  sim('terminalphaseguidancemodel3d')
27  LOSv=lambda_v(end);
28  LOSh=lambda_h(end);
29  if offsetconstant==0
30      offsetLOS=sqrt(25*(t_tgt(Npip)-(t_tgt(end)-t_tgt(1))*0.1667)^2+914^2);
31  end
32  %Introduce target offset perpendicular to lambda_v and lambda_h
33  xo=-offsetLOS*(sin(LOSh)+sin(LOSv)*cos(LOSh));
34  yo=offsetLOS*(cos(LOSh)-sin(LOSv)*sin(LOSh));
35  zo=offsetLOS*cos(LOSv);
36  x0t=x0t-xo;
37  y0t=y0t-yo;
38  z0t=z0t-zo;
39
40  %Simulation
41  RTM_guidance=RIR;
42  sim('terminalphaseguidancemodel3d')
43
44  %Find start conditions for guidance model
45  x0m=xm(end-1);
46  y0m=ym(end-1);
47  z0m=zm(end-1);
48  Vx0m=-vxm(end-1);
49  Vy0m=-vym(end-1);
50  Vz0m=-vzm(end-1);
51  x0t=xt(end-1);
52  y0t=yt(end-1);
53  z0t=zt(end-1);
54  Vx0t=-vxt(end-1);
55  Vy0t=-vyt(end-1);
56  Vz0t=-vzt(end-1);
57  LOS0v=lambda_v(end-1);
58  LOS0h=lambda_h(end-1);
```

Listing C.6: m-file 'driverfile3D.m'.

```matlab
1   %Driverfile missile guidance in 3D
2
3   %Guidance parameters
4   Tc=0.5;                    %Timeconstant autopilot interceptor [s]
5   N=3;                       %Eff. nav. ratio for ballistic trajectories [-]
6   %Simulation
7   te=4000;                   %Max. length simulation [s]
8   dtmax=0.0001;              %Max. length timestep [s]
9   T0=0;                      %Start of simulation [s]
10  sim('terminalphaseguidancemodel3d')
11
12  %Postprocessing
13  miss=min(RTM);
14  dV=sqrt(dVh.^2+dVv.^2);
15  na=sqrt(nah.^2+nav.^2);
```

C.3 Simulink®-file 'terminalphaseguidancemodel2d.slx'
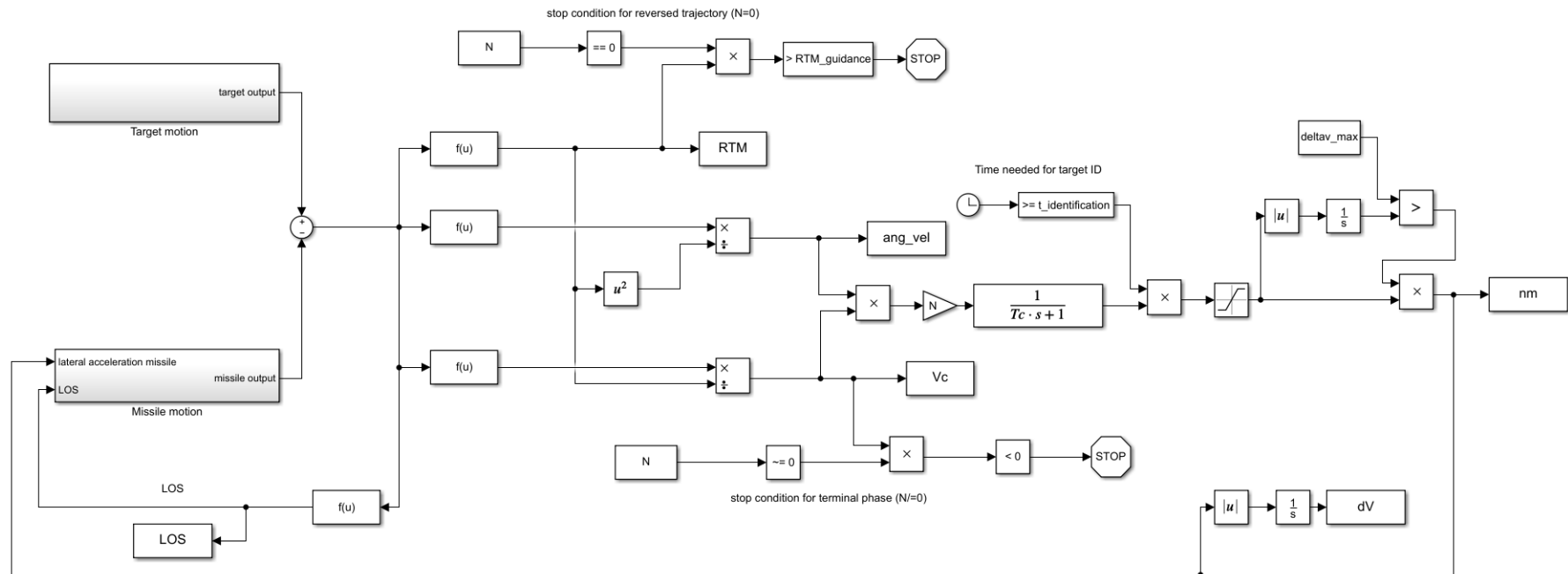
Figure C.1: Main guidance model 2D.
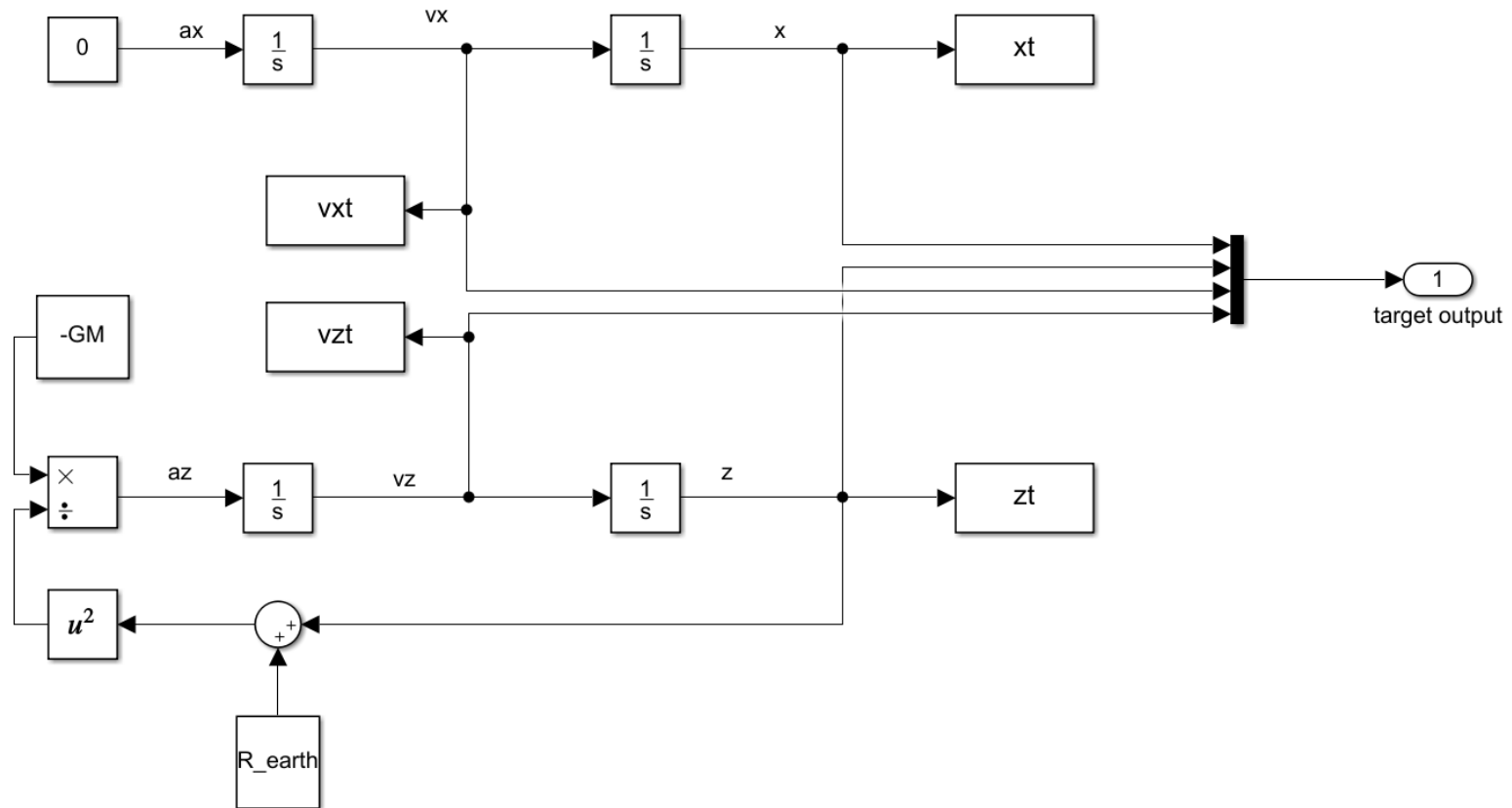
Figure C.2: Target motion submodel 2D.
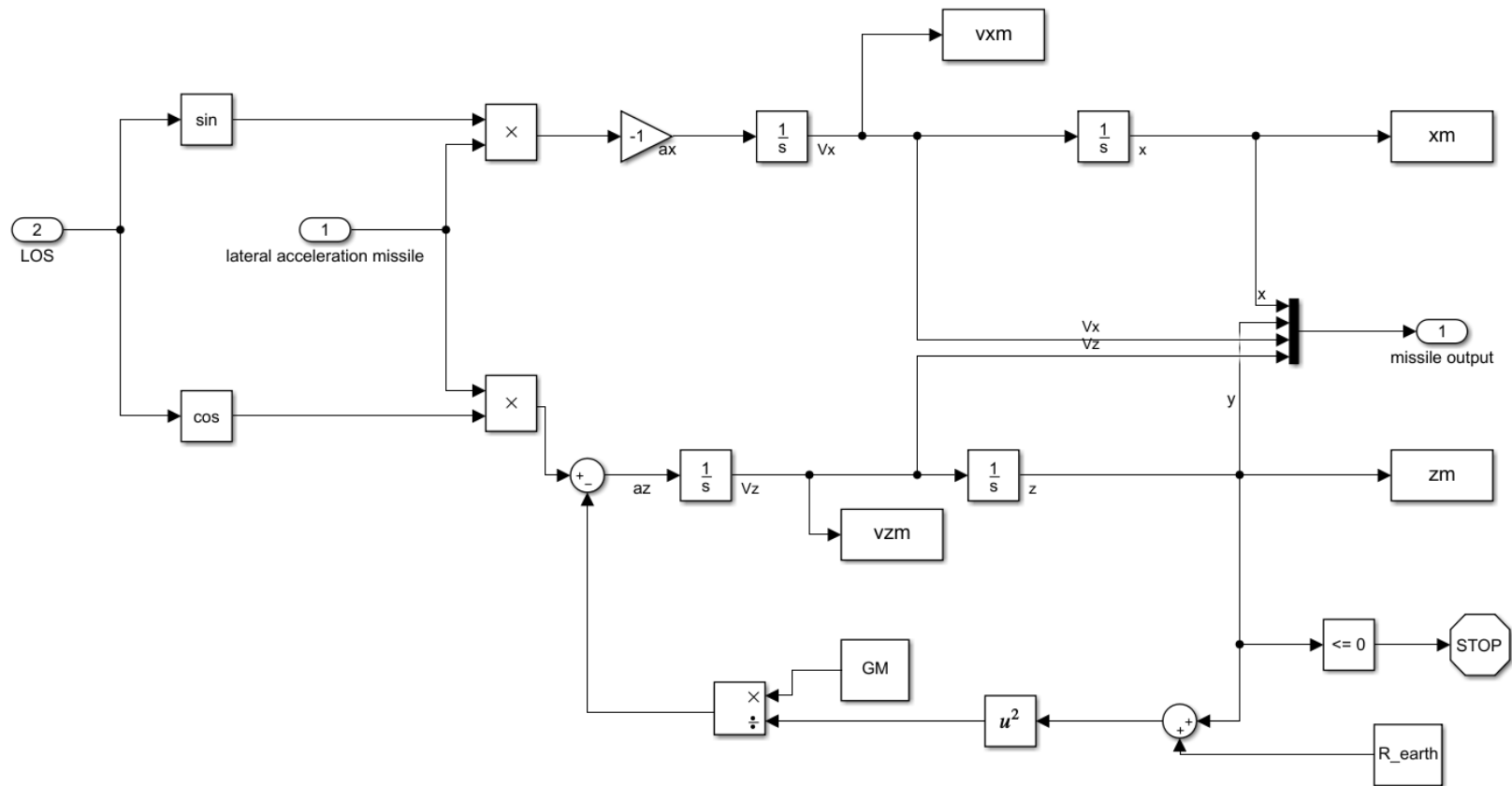
Figure C.3: Missile motion submodel 2D.

C.4 Simulink®-file 'terminalphaseguidancemodel3d.slx'
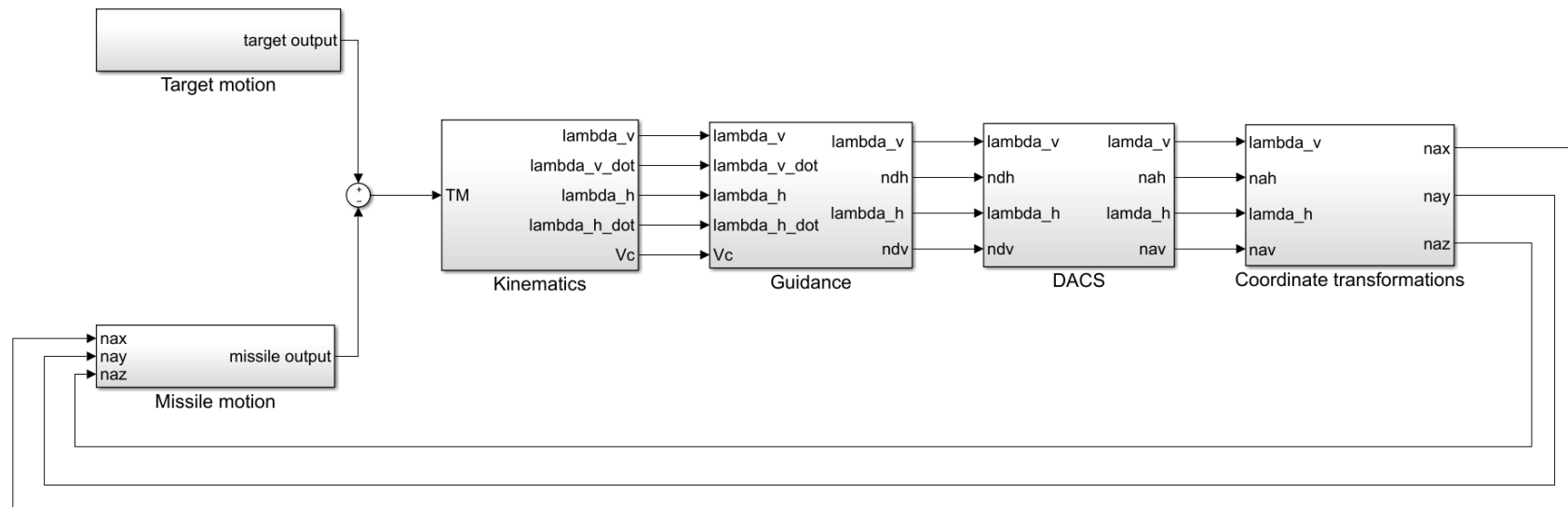
Figure C.4: Main guidance model 3D.
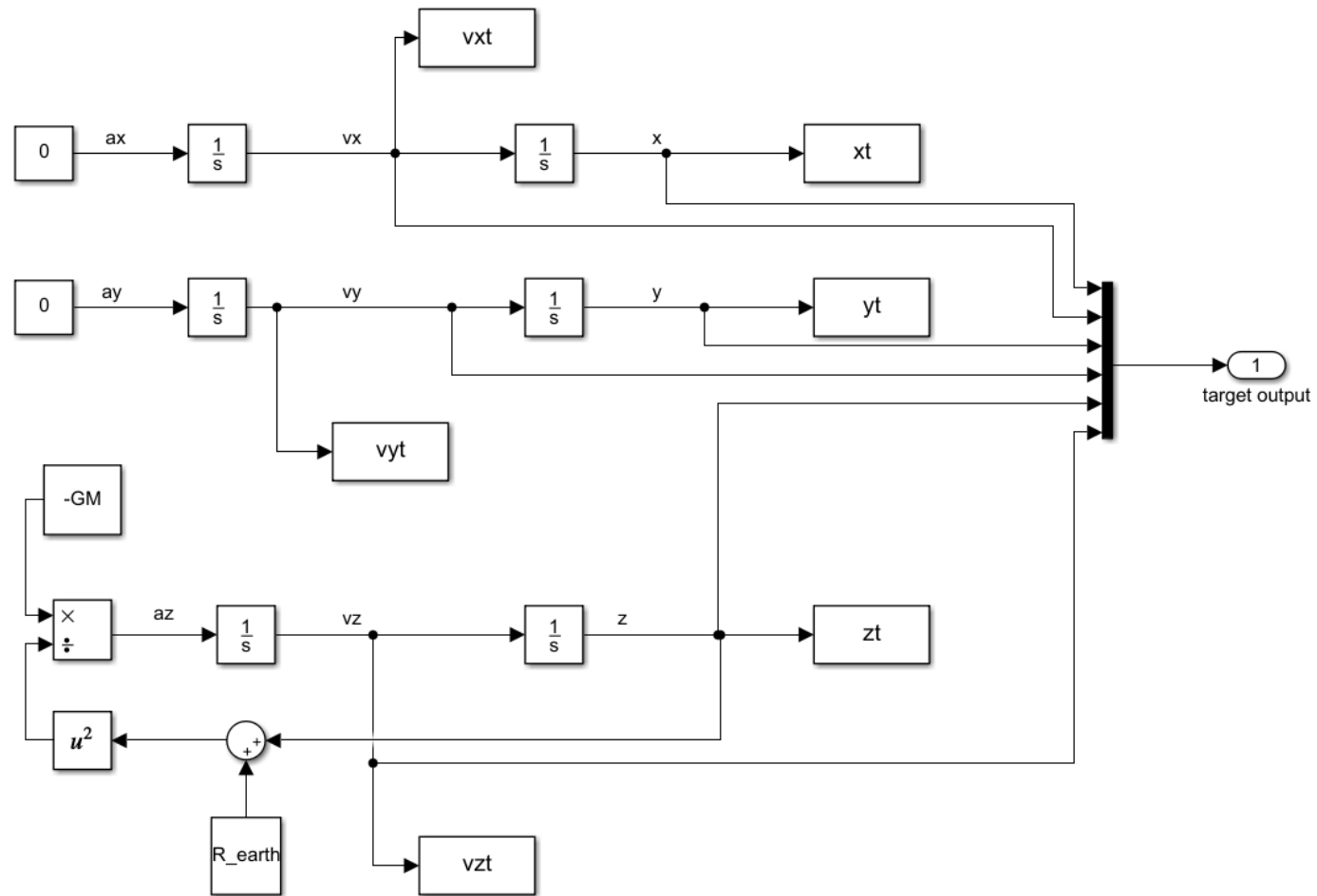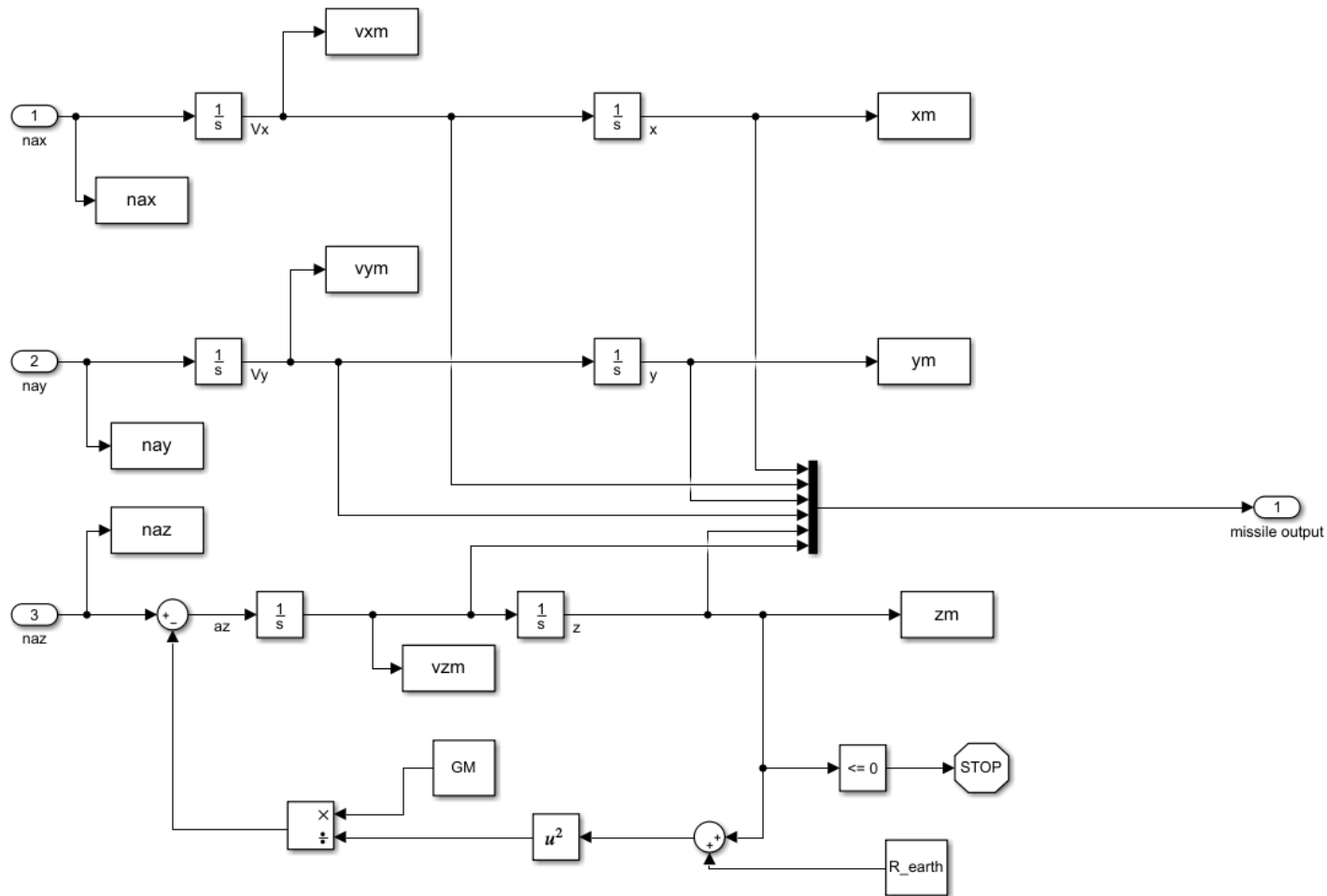
Figure C.5: Target motion submodel 3D.
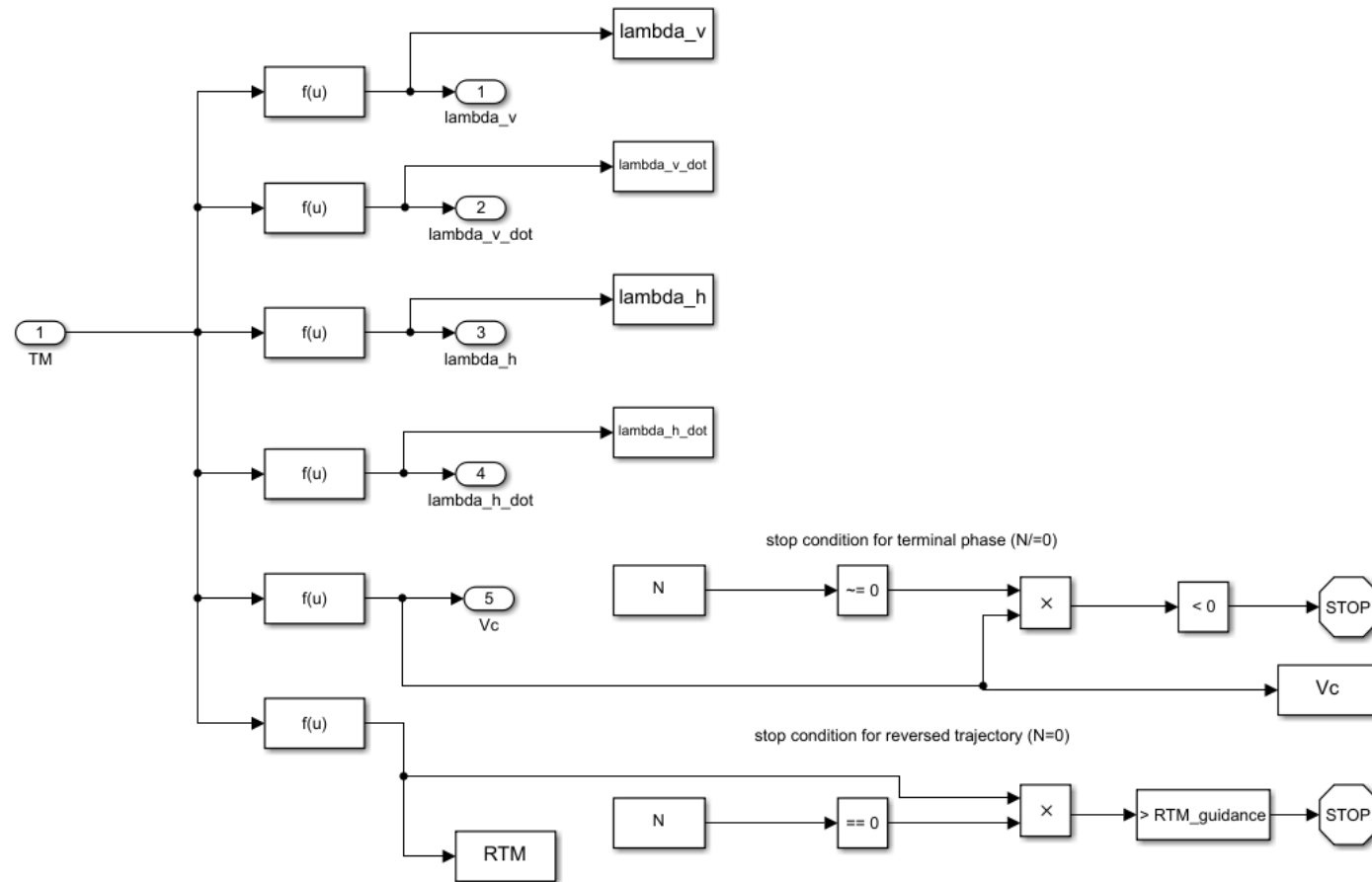
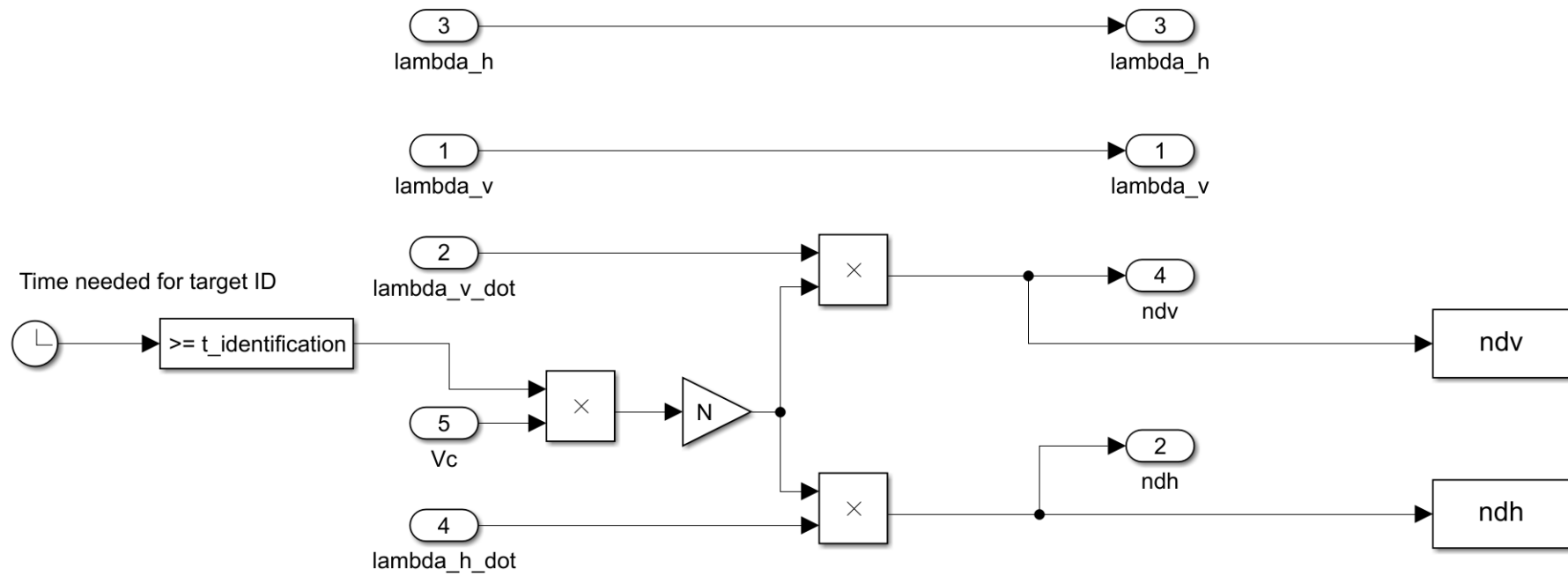Figure C.6: Missile motion submodel 3D.

Figure C.7: Kinematics submodel 3D.
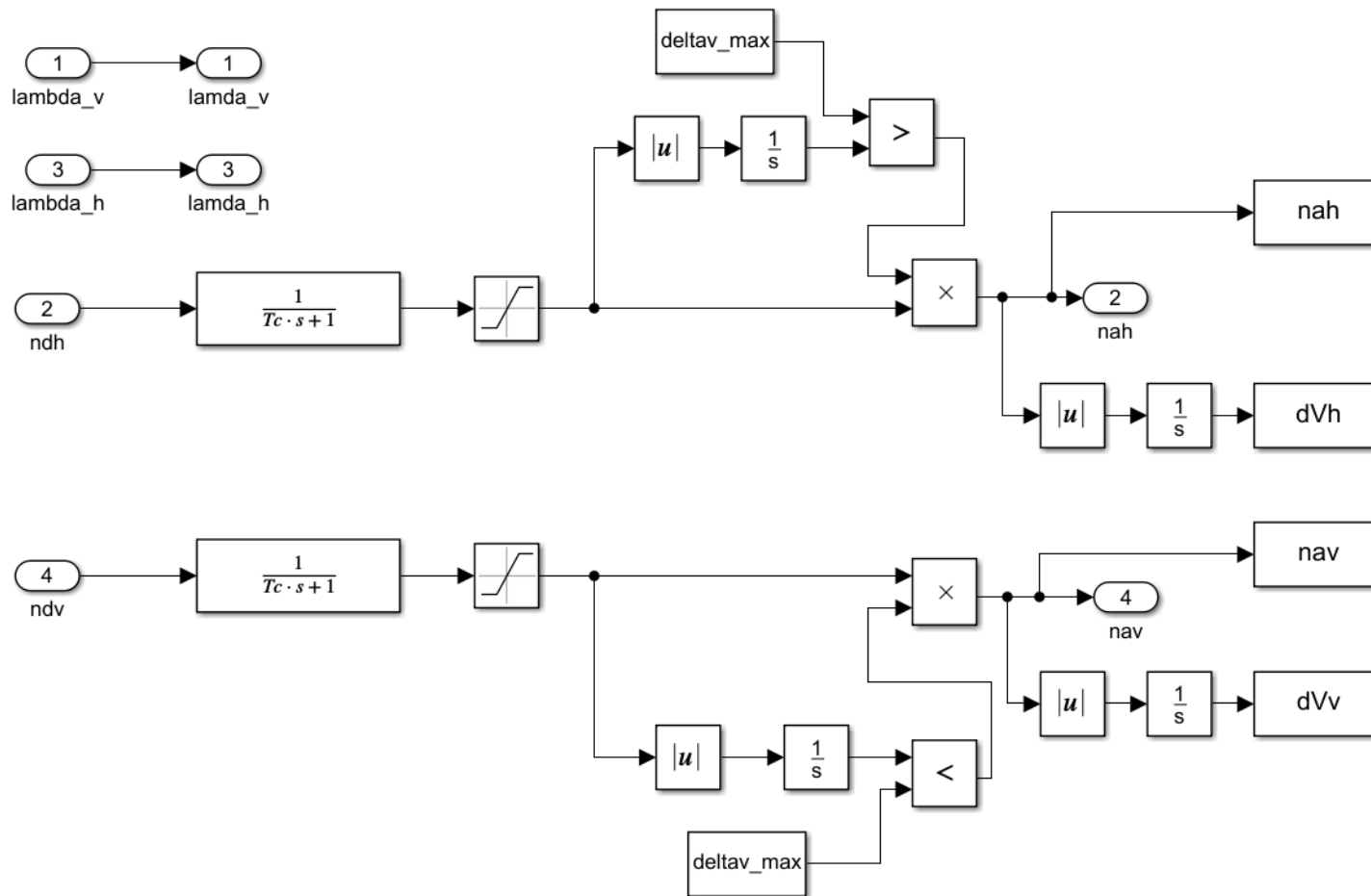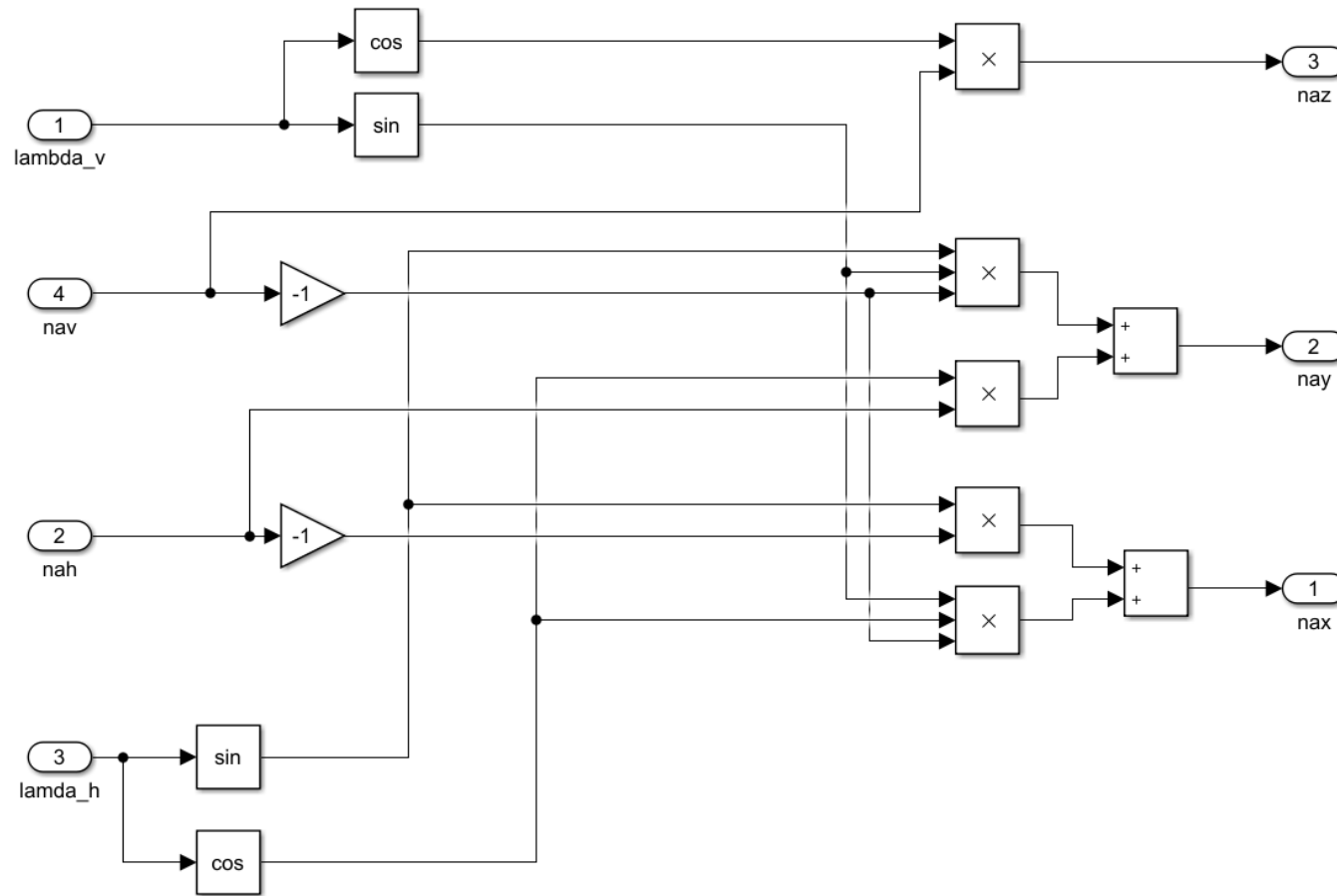
Figure C.8: Guidance submodel 3D.

Figure C.9: DACS submodel 3D.

Figure C.10: Coordinate transformations submodel 3D.